Properties of black carbon and other insoluble light-absorbing particles in seasonal snow of northwest China

5   Wei Pu[1], Xin Wang[1], Hailun Wei[1], Yue Zhou[1], Jinsen Shi[1], Zhiyuan Hu[1], Hongchun Jin[1],

Quanliang Chen[2]

[1] Key Laboratory for Semi-Arid Climate Change of the Ministry of Education, College of Atmospheric Sciences, Lanzhou University, Lanzhou, 730000, China

10   [2] College of Atmospheric Science, Chengdu University of Information Technology, and Plateau Atmospheric and Environment Laboratory of Sichuan Province, Chengdu 610225, China

Correspondence to: Xin Wang (wxin@lzu.edu.cn)

Submitted to The Cryosphere

Abstract. A large field campaign was conducted and 284 snow samples were collected at 38 sites in Xinjiang Province and 6 sites in Qinghai Province across northwestern China from January to February 2012. A spectrophotometer combined with chemical analysis was used to measure the insoluble light-absorbing particles (ILAPs) and chemical components in seasonal snow. The results indicate that the cleanest snow was found in northeastern Xinjiang along the border of China, and it presented an estimated black carbon (C_{BC}^{est}) of approximately 5 ng g^{-1}. The dirtiest snow presented a C_{BC}^{est} of approximately 450 ng g^{-1} near industrial cities in Xinjiang. Overall, the C_{BC}^{est} of most of the snow samples collected in this campaign was in the range of 10-150 ng g^{-1}. Vertical variations in the snowpack ILAPs indicated a probable shift in emission sources with the progression of winter. An analysis of the fractional contributions to absorption implied that organic carbon (OC) dominated the 450-nm absorption in Qinghai, while the contributions from BC and OC were comparable in Xinjiang. Finally, a Positive Matrix Factorization (PMF) model was run to explore the sources of particulate light absorption, and the results indicated an optimal three-factor/source solution that included industrial pollution, biomass burning, and soil dust.

1 Introduction

The deposition of insoluble light-absorbing particles (ILAPs), primarily black carbon (BC), organic carbon (OC), and dust, on snow can reduce snow albedo (Warren and Wiscombe, 1980; Chylek et al., 1983; Brandt et al., 2011; Hadley and Kirchstetter, 2012), which can significantly affect regional and global climate (Jacobson, 2002, 2004; Hansen and Nazarenko, 2004; Flanner et al., 2007, 2009; McConnell et al., 2007; Ramanathan and Carmichael, 2008; Bond et al., 2013). Warren and Wiscombe (1980) indicated that a mixing ratio of 10 ng g^{-1} of BC in snow with snow grain size of 1000 μm may reduce the snow albedo at 400 nm by approximately 1%. A modeling study indicated that soot could reduce snow and sea ice albedo by 0.4% from the global average and by 1% in the Northern Hemisphere (Jacobson, 2004). Previous studies found that the "efficacy" of BC/snow forcing in the Arctic is more than three times greater than that of forcing by CO_2 (Hansen and Nazarenko, 2004; Flanner et al., 2007). However, the regional and global radiative forcing affected by the ILAPs in snow/ice is still a challenge. For instance, Hansen and Nazarenko (2004) found that the effect of soot on snow and ice albedo yielded a climate forcing of +0.3 W m^{-2} in the Northern Hemisphere. Recently, the IPCC's AR5 (2013) reported that the radiative forcing from BC in snow and ice is 0.04 W m^{-2} of the global mean, although it presents a low confidence level. Bond et al. (2013) indicated that the best estimate of climate forcing from BC deposition on snow and sea ice in the industrial era is +0.13 W m^{-2} with 90% uncertainty bounds of +0.04 to +0.33 W m^{-2}. The all-source present-day climate forcing including preindustrial emissions is somewhat higher at

+0.16 W m^{-2}. However, recent studies indicated that many factors complicate the evaluation of climate forcing by BC in snow (Hansen and Nazarenko, 2004; Bond et al., 2013). Hence, abundant comprehensive field campaigns are required to collect snow samples and measure ILAPs in snow to limit this uncertainty.

5 Recently, a number of field campaigns have been conducted to measure the BC in snow and ice in the Arctic (Clarke and Noone, 1985; Chylek et al., 1987, 1995; Cachier and Pertuisot, 1994; Grenfell et al., 2002; Hagler et al., 2007a, 2007b; McConnell et al., 2007; Forsstrom et al., 2009; Doherty et al., 2010, 2013). Overall, the BC mixing ratios in the snow of the Arctic were 3-30 ng g^{-1}. The cleanest snow

10 was found on the Greenland Ice Sheet, whereas the dirtiest snow was found in East Russia (Doherty et al., 2010). Modeling studies have also evaluated the effect of BC in snow on warming in the Arctic (Hansen and Nazarenko, 2004; Jacobson, 2004; Flanner et al., 2007, 2009; Koch et al., 2009; Shindell and Faluvegi, 2009). Hansen and Nazarenko (2004) suggested that the mean effect of soot on the spectrally

15 integrated albedos in the Arctic is 1.5%. Flanner et al. (2007) noted that the simulated annual Arctic warming is 1.61°C and 0.50°C for 1998 and 2001 central experiments when BC is included in snow compared with control simulations without BC. However, limited field campaigns and modeling studies are available in North America (Chylek et al., 1987; Qian et al., 2009; Hadley et al., 2010; Dang and Hegg,

20 2014; Doherty et al., 2014), Europe (Eleftheriadis et al., 2009; Thevenon et al., 2009; Painter et al., 2013; Gabbi et al., 2015; Peltoniemi et al., 2015), the Tibetan Plateau (Xu et al., 2006, 2009, 2012; Kang et al., 2007; Ming et al., 2008, 2009; Qiu, 2008;

Cong et al., 2013; Wang et al., 2014; Li et al., 2016), and North China (Huang et al., 2011; Ye et al., 2012; Wang et al., 2013; Zhao et al., 2014), where snow is closer to the sources of ILAPs and more exposed to sunlight; therefore, the effect of ILAPs on snow may be more significant. Hence, we conducted a large field campaign to measure the ILAPs in seasonal snow across northwestern China from January to February 2012.

In addition to BC, which presented the most absorptive impurity per unit mass, OC and dust can also significantly contribute to particulate light absorption in snow. OC in snow may be related to either combustion products that are deposited onto snow or soil that is mixed into snow. Xu et al. (2006) first quantified the OC content on the Tibetan Plateau and determined the effect of OC on surface snow melting. Wang et al. (2013) suggested that OC dominates the particulate light absorption across the grasslands of Inner Mongolia in North China. Recent studies have indicated that the light absorption by mineral dust is mainly related to iron oxides such as goethite and hematite (Alfaro et al., 2004; Lafon et al., 2004, 2006). Although its ability to reduce snow albedo is less than that of BC by approximately a factor of 50 (Warren, 1984). We note that the mass loading of mineral dust could be dominated in several snow sampling locations (Wang et al., 2013). For example, the increased radiative forcing by dust in snow has affected the timing and magnitude of runoff from the Upper Colorado River Basin (Painter et al., 2007, 2010).

Understanding the sources of ILAPs in snow is necessary for examining the climatic effects of ILAPs in snow. Certain scientists have focused on exploring the potential

sources of BC in snow (Flanner et al., 2007; Shindell et al., 2008; Forsstrom et al., 2009); however, these studies primarily relied on numerical transport modeling based on limited datasets from emission inventories or calculated back trajectories, and they showed a limited ability to attribute the sources of BC. Recently, a standard receptor

5 model has been successfully used to resolve the sources of ILAPs in snow. For example, Hegg et al. (2009, 2010) utilized measured ILAPs and chemical components as inputs to run the model. The results showed four sources (crop and grass burning, boreal biomass burning, pollution, and marine) of light-absorbing particles in the Arctic snow. Biomass burning sources dominated during spring, although pollution

10 played a more significant role during fall and winter and in summer in Greenland. Zhang et al. (2013a) evaluated the source attribution of ILAPs in the snow in northeastern China and found three sources for the ILAPs in the snow pack: soil dust (53%), industrial/urban pollution (27%), and biomass and biofuel burning (20%). These authors concluded that soil dust was the dominant source in the northeastern

15 area of China, which is consistent with assessments that were based on back trajectory cluster analyses. A similar study by Doherty et al. (2014) focused on the sources of snow BC in North America and found that both biomass and fossil fuel combustion were the main sources of snow BC in the Pacific Northwest, Intermountain West and Canada, whereas soil dust played a predominant role in particulate light absorption in

20 the northern U.S. Plains. Obviously, analyses based on the receptor model are timely and useful for identifying the source attribution of snow BC; thus, this model can be used to assess the potential sources of ILAPs in the snow in northwestern China

because of the variety of emission sources (Ye et al., 2012).

In this study, we analyzed the spatial and vertical distributions of ILAPs in the seasonal snow across northwestern China to investigate the contributions from BC, OC and Fe to particulate light absorption. The chemical components and ILAPs were also used to estimate the potential emission sources and source attributions of ILAPs in seasonal snow.

2 Methods

2.1 Snow collection

Seasonal snow was collected at 38 sites in Xinjiang and 6 sites in Qinghai in China from January to February 2012, with 284 snow samples obtained across the entire expedition. Figure 1 shows the locations of the sampling sites, which were numbered in chronological order and followed the field campaign by Wang et al. (2013). Fresh snow was gathered from 13 sites where snow was falling at the time of sampling. Forty-two sites were separated into 5 regions according to their geographical distribution to investigate the spatial variations in snow-containing contaminants and their potential sources, with Region 1 in Qinghai and Regions 2-5 in Xinjiang.

Normally, snow samples were collected at vertical intervals of 5 cm from the top to the bottom at each site. If distinct layering was present, such as a melt layer or a top layer of newly fallen snow, that layer was collected individually. In Qinghai, the snow was thin and patchy at sites 47-49; therefore, the samples were collected from drift snow. Left and right snow samples were gathered within each layer in two adjacent vertical profiles to compare and average the sample pairs. Snow density and snow

temperature were also measured within each layer, which could be useful for the parameterization of snow albedo modeling (Flanner et al., 2007, Wang et al., 2017). The sampling sites were selected 50 km far from cities and at least 1 km upwind of the approach road or railway to minimize the effect of pollution from local sources and achieve a representation of large areas.

The snow samples were filtered at four temporary laboratories to prevent the melting snow from influencing the ILAPs content. The snow samples were quickly melted in a microwave oven and then immediately filtered through a 0.4-μm Nuclepore filter. The samples "before" and "after" filtration were collected and refrozen for subsequent chemical analyses, and the filters were used to measure the light absorption of ILAPs. Additional details on the snow collection and filtration processes have been previously reported (Doherty et al. 2010, 2014; Wang et al., 2013).

2.2 Chemical speciation

The chemical analysis performed here followed that of Wang et al. (2015) and was similar to the procedures described by Zhang et al. (2013a) and Doherty et al. (2014). Details of these approaches have been previously reported by Yesubabu et al. (2014). Briefly, the major ions (SO_4^{2-}, NO_3^-, Cl^-, F^-, Na^+, K^+, Ca^{2+}, Mg^{2+} and NH_4^+) were analyzed with an ion chromatograph (Dionex, Sunnyvale, CA, USA), and the trace elements (e.g., Fe, Al, Cu, Mn, Cr, and Ba) were measured by inductively coupled plasma mass spectrometry (ICP-MS). Pairs of unfiltered and filtered snow water samples were analyzed to evaluate the possible effect of filtering on the chemical constituents, and obvious differences were not observed. Mineral dust (MD), Cl salt,

biosmoke K ($K_{Biosmoke}$) and trace element oxides (TEO) were determined to assess the mass contributions of the major components in the surface snow. The mineral dust content was calculated by a straightforward method, and the Al concentration in dust was estimated at 7% (Zhang et al., 2013b):

$$MD=Al/0.07 \tag{1}$$

Cl salt was estimated as follows in accordance with Pio et al. (2007) and Zhang et al. (2013b):

$$Cl\ salt=Na_{Ss}^{+}+Cl^{-}+Mg_{Ss}^{2+}+Ca_{Ss}^{2+}+K_{Ss}^{+}+SO_{4Ss}^{2-}$$

$$=Na_{Ss}^{+}+Cl^{-}+0.12Na_{Ss}^{+}+0.038Na_{Ss}^{+}+0.038Na_{Ss}^{+}+0.25Na_{Ss}^{+} \tag{2}$$

where Na_{Ss}^{+} is sea salt Na^{+}, 0.12, 0.038, 0.038, and 0.25 are the mass ratios in seawater of magnesium to sodium, calcium to sodium, potassium to sodium and sulfate to sodium, respectively. Na_{Ss}^{+} is calculated as follows (Hsu et al., 2009):

$$Na_{Ss}=Na_{Total}-Al*(Na/Al)_{Crust} \tag{3}$$

where $(Na/Al)_{Crust}$ is the Na/Al ratio of representative dust materials (Wedepohl, 1995). Following Hsu et al. (2009), we estimated all three fractions (dust, sea salt, and biosmoke fractions) of K in snow, and $K_{Biosmoke}$ was determined as follows:

$$K_{Biosmoke}=K_{Total}-K_{Dust}-K_{Ss} \tag{4}$$

$$K_{Dust}=Al*(K/Al)_{Crust} \tag{5}$$

$$K_{Ss}=Na_{Ss}*0.038 \tag{6}$$

where $(K/Al)_{Crust}$ is 0.37 and represents the K/Al ratio in the dust materials (Wedepohl, 1995) and Na_{Ss} is estimated by Equation (3). Following Zhang et al. (2013b), we calculated the contribution of TEO using the following equation:

$$TEO=1.3*\sum_i(\alpha_i*TE_i) \tag{7}$$

where TE represents the trace elements (Ti, V, Cr, Mn, Co, Ni, Cu, Zn, As, Se, Sr, Mo, Ag, Cd, Sn, Ba, Hg, Tl, Pb, Th, U, and Be) determined via ICP-MS and α is the weight coefficient of each trace element. α is a function of the enrichment factor (EF):

$\alpha=0$, $EF\leq1$;

$\alpha=0.5$, $1<EF<5$; $\tag{8}$

$\alpha=1$, $EF\geq5$.

where the EF of a given element (E) is calculated by the equation $EF=(E/Al)_{Snow}/(E/Al)_{Crust}$ (Hsu et al., 2010). $(E/Al)_{Snow}$ and $(E/Al)_{Crust}$ are the ratios of the elements to the Al concentration in the snow sample and crust (Wedepohl, 1995), respectively. A multiplicative factor of 1.3 was used to convert the element abundance to the oxide abundance, which is similar to the method of Landis et al. (2001).

2.3 Spectrophotometric analysis

The filters were analyzed for the ILAPs content in the snow using a modified integrating-sandwich spectrophotometer (ISSW), which was described by Grenfell et al. (2011) and performed by Doherty et al. (2010, 2013, 2014, 2015), Dang and Hegg (2014) and Wang et al. (2013, 2015). This ISSW spectrophotometer measures the light attenuation spectrum from 400 to 700 nm where the signal-to-noise ratio is optimized. The total light attenuation spectrum is extended over the full spectral range by linear extrapolation from 400 to 300 nm and from 700 to 750 nm (Grenfell et al., 2011).

Light attenuation is nominally only sensitive to ILAPs on the filter because of the diffuse radiation field and the sandwich structure of two integrated spheres in the ISSW (Doherty et al., 2014). By considering all of the light absorption that occurred from 650-700 nm, the maximum possible BC (C_{BC}^{max}) mixing ratio was calculated by calibrating the results against a set of fullerene (Alfa Aesar, Inc., Ward Hill, MA, USA) standard filters with a mass absorbing coefficient (MAC) of 6.3 m^2 g^{-1} at 550 nm. In general, BC, OC and dust (Fe) dominated the light absorption by ILAPs in the snow samples. The equivalent BC (C_{BC}^{equiv}), estimated BC (C_{BC}^{est}), absorption Ångström exponent of all ILAPs ($Å_{tot}$), and light absorption fraction by non-BC ILAPs (f_{nonBC}^{est}) were calculated by using the wavelength dependence of the measured spectral light absorption and by assuming that the MACs of the BC, OC and Fe were 6.3, 0.3, and 0.9 m^2 g^{-1} at 550 nm, respectively, and that the absorption Ångström exponents (Å or AAE) were 1.1, 6, and 3, respectively. The description of these variables could be found in Table 1. The details of this analysis were interpreted according to Grenfell et al. (2011). The OC mixing ratio was also determined according to Equation (2) in Wang et al. (2013), and the Fe concentration was determined according to the ICP-MS measurements.

Many studies (e.g., Jacobson, 2001; Hadley and Kirchstetter, 2012; Bond et al., 2013) have indicated that the MAC of BC is somewhat higher than the value used here, and Bond and Bergstrom (2006) recommended a value of 7.5±1.2 m^2 g^{-1} at 550 nm. However, we applied a value of 6.3 m^2 g^{-1} to provide a comparison with previous studies (Hegg et al., 2009, 2010; Doherty et al., 2010; Wang et al., 2013). If the MAC

of BC is actually close to 7.5 m^2 g^{-1}, then our measured mass mixing ratio will be too high by a factor of 1.19. If the radiation models are run with the BC mixing ratio reported in this study, then the MAC of BC must be 6.3 m^2 g^{-1}; otherwise, the BC mixing ratio should be scaled appropriately.

2.4 PMF model

The Positive Matrix Factorization (PMF) model that was used here (US EPA PMF 5.0) is a receptor model that provides source attribution by identifying and quantifying source profiles and contributions prior, which is based on mathematical approaches, and it has been widely applied (e.g., Amato et al., 2009; Amato and Hopke, 2012). The speciation or composition is determined by using analytical methods appropriate for the media, and key component or combinations of components are required to distinguish the effects. The PMF model is a multivariate factor analysis tool that decomposes a matrix of speciated sample data into two matrices: factor contributions and factor profiles. These factor profiles must be interpreted by the analyst to identify the source types that may have contributed to the sample by using available ancillary information, such as the measured source profile information and emission or discharge inventories. The characteristic factor profiles are completely dependent on the mathematical approaches of the PMF model; therefore, the number of factors is unknown priori, which must be selected individually in terms of stability, accuracy, performance, and geochemical likeliness of the PMF results and the analyst's understanding of the sources.

Normally, the PMF model is applied to analyze a time series of components

concentrations at a single observation site to estimate temporal variations. In this study, we used the PMF model to analyze the spatial variations in source contributions. Although atypical, previous studies have effectively employed this model and confirmed its reliability in terms of factor analyses of spatial distributions (Paatero et

5   al., 2003; Chen et al., 2007; Hegg et al., 2009, 2010; Zhang et al., 2013a; Doherty et al., 2014).

3 Results

Table 2 summarizes the 2012 northwestern China field campaign and lists the values for the C_{BC}^{equiv}, C_{BC}^{max}, C_{BC}^{est}, $Å_{tot}$, and f_{nonBC}^{est} at every sampling layer for each site. The

10 cleanest snow was found in the far north of Xinjiang Province (sites 70, 75, 77 and 78) and the high-altitude sites in the Tianshan Mountains (sites 79 and 82) because these sites were located far from the emission sources; moreover, the melting-amplified effect on the BC mixing ratios was negligible because the field campaign was conducted in January and February when the snow had not yet melted. Although the

15 C_{BC}^{est} result was low and reached values of 1 ng g^{-1} at site 77, the C_{BC}^{est} estimates were considered too uncertain when the corresponding f_{nonBC}^{est} was > 85% according to Doherty et al. (2014); therefore, we did not consider these values. Thus, the lowest C_{BC}^{est} values were approximately 5 ng g^{-1}, which were smaller than the minimum BC mixing ratio of approximately 40 ng g^{-1} measured in North China via the same

20 spectrophotometric analysis (ISSW) (Huang et al., 2011; Wang et al., 2013) and comparable to the values of approximately 3 ng g^{-1} from the Greenland Ice Sheet (Doherty et al., 2010). The highest C_{BC}^{est} was found at sites 53, 60, 67, 83 and 84. At

site 83, the C_{BC}^{est} reached 619 ng g^{-1} at the bottom layer; however, the underlying soil may have been responsible for this high value. Therefore, we note that this value should not be used to represent the regional background level of BC. After excluding the bottom value of C_{BC}^{est} at site 83, the highest C_{BC}^{est} value was approximately 450 ng

5   g^{-1}, which was much lower than the values of $>$1000 ng g^{-1} in snow in the industrial area of northeastern China (Wang et al., 2013). Overall, the C_{BC}^{est} of most of the snow samples ranged from 10-150 ng g^{-1}, which were similar to the values by visual estimates reported by Ye et al. (2012), and BC measurements of 4-120 ng g^{-1} recorded from glaciers in Tibet and Xinjiang by the previous field campaigns that used a

10   controlled combustion method (Xu et al., 2006, 2009; Ming et al., 2008, 2009).

3.1 Results by region

As discussed above, the sample sites were separated into five regions. Table 3 lists the regional averages and standard deviations of C_{BC}^{equiv}, C_{BC}^{max}, C_{BC}^{est}, $Å_{tot}$, and f_{nonBC}^{est} for the surface and subsurface layers. The spatial distributions of C_{BC}^{est} and $Å_{tot}$ for the

15   surface snow samples are shown in Figure 2a and 2b. In addition, Figure 2c shows the equivalent BC value used to explain the 300-750-nm absorption by all non-BC ILAPs, which was calculated as $C_{BC}^{equiv} * f_{nonBC}^{est}$. Thus, Figures 2a and 2c can be compared to determine the relative contributions from BC and non-BC ILAPs to the snow albedo reduction at each site. However, the BC mass deposited onto snow over a specified

20   period is more useful when comparing models than the surface values because the average BC over many snowfall events across a typical month or season presents a more representative contribution to the background levels throughout the entire

accumulation period (Doherty et al., 2014). Thus, the integrated snow water equivalent (SWE) and the total BC mass for a 1-cm^2 column of snow (integrated BC) were given in table 4. We also estimated the average BC mixing ratios in the snow column ($\overline{C_{BC}^{est}}$), which were calculated as the integrated BC divided by the SWE (Figure 2d and Table 4). Indeed, the $\overline{C_{BC}^{est}}$ value was more spatially uniform than the C_{BC}^{est} value.

In Region 1 (sites 47-52), which is located in the eastern Tibetan Plateau in Qinghai Province, the snow was thin and patchy and presented a sample snow depth of 2.5-10 cm. During windy periods, local soil can be lofted and deposited onto snow surface, and this deposition has been confirmed by previous reports (Ye et al., 2012), which shown as yellowed filters because of the heavy loading of soil dust. Although the C_{BC}^{est} was intermediate and presented typical values of 30-150 ng g^{-1}, both the C_{BC}^{equiv} and $C_{BC}^{equiv} * f_{nonBC}^{est}$ values were highest in the surface (307±119, 213±89 ng g^{-1}) and subsurface (332±201, 214±116 ng g^{-1}) snow among all five regions (Table 3 and Figure 2) when considering the primary proportion of non-BC ILAPs in the mass of the ILAPs. In addition, the Å$_{tot}$ values were 3.6-4.6 and higher than those in any other region, which indicated the predominant contribution from non-BC ILAPs to light absorption.

Region 2 (sites 53-59, 61, and 79) is located on the Tianshan Mountains, and except for site 58, all of the sites were located far from cities. Site 58, which is situated in the foothills near Yili prefecture, likely experiences a greater influence of human activities. All of the regional statistics were intermediate. The C_{BC}^{est} values were

generally in the range of 20-100 ng g^{-1}. At site 54, the surface C_{BC}^{est} was low and

reached 7 ng g^{-1}. Higher altitudes (> 3000 m) and freshly fallen snow at the surface

may have been responsible for this lower value. The higher mixing ratios at site 53 for

both surface and subsurface snow may have been caused by local soil dust or biomass

5   burning as reported by Ye et al. (2012). The $Å_{tot}$ values varied remarkably from 2.2

to 4.5.

Region 3 (sites 60, 62-63, and 80-84) is located to the north of the Tianshan

Mountains, and industrial cities are located close to this region, and the population

density is much higher than that in any of the other regions; therefore, human

10   activities may have dominated the contributions to ILAPs in the snow. However, the

C_{BC}^{est} values, which primarily ranged from 10-100 ng g^{-1}, were comparable to those in

other regions in Xinjiang, which were inconsistent with the findings in North China,

where the C_{BC}^{est} in the industrial northeastern area was higher by a factor of 10

compared with the values to the remote northeast on the border of Siberia (Wang et al.,

15   2013). The f_{nonBC}^{est} for the surface and subsurface samples was considerable different

and presented values of 58±15% and 72±12%, respectively, which reflects the

temporal changes in the contributions from BC and non-BC particles to light

absorption over time. The $Å_{tot}$ values were typically 2-4, which were comparable to

those in Region 2, despite the snow samples may have been more affected by human

20   activities.

Region 4 (sites 64-70) is located in northwestern Xinjiang along the border of China.

The C_{BC}^{est} generally ranged from 20-150 ng g^{-1}. The regional average $Å_{tot}$ was

approximately 3. The f_{nonBC}^{est} in this region was the lowest and presented an average value near 50%; therefore, the BC and non-BC particles presented almost identical contributions to light absorption, which was inconsistent with the other regions, where non-BCs played a dominant role.

5 The cleanest snow of this campaign was found in Region 5 (sites 72-78) in northeastern Xinjiang. Most of the snow samples had low C_{BC}^{est} values of 10-50 ng g^{-1}, which were much smaller than the values of 50-150 ng g^{-1} in the cleanest snow in northeastern China. The $Å_{tot}$ value generally ranged from 2.5 to 3.5 and presented a regional average of approximately 3, which was consistent with other regions in

10 Xinjiang. The f_{nonBC}^{est} varied obviously varied from < 50% to > 90%. This wide range indicates the spatial variance in the dominant emission sources of particulate light absorption in this region.

3.2 Vertical variations in snowpack light-absorbing particulates

The vertical profiles of the C_{BC}^{max}, C_{BC}^{est}, and $Å_{tot}$ at each sample site are shown in

15 Figure 3. At sites 49-52 in Qinghai (Region 1), an obvious dust layer was present in each site, and analyses of the ILAPs content by ISSW presented high uncertainties. Therefore, we did not report the values at these layers. In addition, the sampling at sites 47-49 was conducted in drift snow as discussed above. Thus, the vertical profiles from these sites in Qinghai did not accurately represent the temporal variations in the

20 deposition of snow, although apparent vertical differences could be observed at could sites, such as site 47. In Regions 3, 4 and 5 in Xinjiang, the C_{BC}^{est} values were much larger in the surface snow (127±158, 126±124, and 74±56 ng g^{-1}, respectively) than in

the subsurface snow (75±120, 82±56, and 37±31 ng g^{-1}, respectively), with the ratio

of the C_{BC}^{est} from the top layer to the average C_{BC}^{est} from all the subsurface layers

presenting values of 1.7, 1.5, and 2, respectively, which indicates an increase in

aerosol deposition later in winter. However, the C_{BC}^{est} values in the surface (81±102

5   ng g^{-1}) and subsurface layers (89±69 ng g^{-1}) in Region 2 were comparable. These

differences in deposition could have been caused by changes in the dry deposition

and/or the mixing ratio of the ILAPs to the precipitation water content in snowfall.

Doherty et al. (2013) studied the observed vertical redistribution of BC and other

ILAPs in melting snow and noted that melt amplification generally appears within the

10   top few centimeters of the snowpack, and it increases the BC mixing ratios of the

surface snow. However, the high surface BC values reported here could not have

originated from this mechanism because the temperature at these sites was not high

enough to melt the snow. The $Å_{tot}$ and f_{nonBC}^{est}, the values increased by 0.41 and 10%

from the subsurface to the surface snow in Region 2, respectively, but decreased by

15   0.40 and 14% in Region 3, respectively. These variations may have been partly caused

by a shift in emission sources as winter progressed, with a greater contribution to the

ILAPs in snow from biomass burning in Region 2 and fossil fuel burning in Region 3

during this season.

3.3 Contributions to particulate light absorption by BC, OC and Fe

20   Figure 4a shows the fractional contributions of BC, OC and Fe to light absorption at

450 nm for the surface snow samples at each site. In Qinghai (Region 1), OC

dominated the absorption, and the fractional contribution reached approximately 70%.

However, dust accounted for the main portion of the particulate mass, which was confirmed by the yellow color of the filters, and the fractional contribution from Fe to absorption (only approximately 5%) was not significant. In Xinjiang, the fractional contributions from BC, OC and Fe were approximately 45%, 50%, and 5%, respectively, and their patterns did not vary greatly by region. At sites 58, 75, and 77, the fraction of light absorption from Fe exceeded 20%. This value was much higher than the values at the other sites, which may be explained by two possible reasons: (1) less BC and OC were contributed by biomass and fossil fuel burning and more Fe was contributed by dust, and (2) Fe was contributed by industrial emissions as well as dust. Wang et al. (2013) analyzed the snow particulate light absorption by ILAPs in the snow samples across northeastern China and noted that OC could be composed of soil organics, combustion aerosols, and/or other biological organics. BC and OC could be produced via combustion sources, such as fossil fuel burning, open burning and biofuel burning. Thus, we could not precisely separate the contributions from different sources by analyzing the ILAPs. Hence, a more feasible method is required to evaluate and quantify the contributions from emission sources to particulate light absorption (see Section 3.4).

The relative contributions of these three components are related to the values of $Å_{tot}$ and $Å_{nonBC}$, which are shown in Figure 4b. Overall, the $Å_{nonBC}$ values were almost in a narrow range of 5-6, which indicated that OC was the major component of non-BC ILAPs because the $Å$ values of OC and Fe were 6 and 3, respectively. Three exceptions were sites 58, 75, and 77, which had $Å_{nonBC}$ of $<$ 5, and higher fractional

contributions from Fe to absorption likely resulted in these lower values. Compared with $Å_{nonBC}$, the $Å_{tot}$ values varied greatly from 1.84 to 4.66, and the large variety of BC mixing ratios was mainly responsible for the large changes in $Å_{tot}$. In terms of the spatial distribution, the $Å_{tot}$ value was close to the $Å_{nonBC}$ value in Qinghai (Region

5   1), although the differences between $Å_{tot}$ and $Å_{nonBC}$ were highly variable in Xinjiang.

As discussed in Section 2.3, we attributed the snow particulate absorption to BC, OC, and Fe based on the absorption optical depth measured by ISSW spectrophotometer along with the chemical analyses of Fe and assumptions for the $Å$ values and mass

10   absorbing coefficients of BC, OC, and Fe. Furthermore, $Å_{nonBC}$ was determined by the light absorption of OC and Fe. However, the assumptions presented large uncertainties, which may have introduced considerable errors in the values of BC, OC, and $Å_{nonBC}$. Doherty et al. (2010) analyzed the errors that originated from these assumptions and indicated a likelihood of uncertainty of < 50% based on liberal

15   evaluations of these potential sources of errors. Lack and Langridge (2013) indicated that the attribution biases of BC absorption are from +7% to −22% by using the AAE in the range of 1.1 ± 0.3 instead of 1 as the common default. In order to reduce the uncertainty of BrC absorption at 404 nm less than ±100%, the absolute contribution from BrC absorption must be at least 23% (10%) of that from BC for PAS

20   measurements. Significantly, the variation of AAE plays an important role in affecting the light absorption attribution. However, most of the studies only took BC and BrC (or OC) into account, which ignored the effect of mineral dust on light absorption. For

instance, Doherty et al. (2010) revealed that the consideration of dust will add the complexity but does not effectively change the results due to negligible fractional light absorption of dust in some areas such as the Arctic. However, Wang et al. (2013) and Zhang et al. (2013a) indicated that the light absorption of mineral dust could not be negligible across northern China.

Therefore, in view of the importance of mineral dust and the complexity of the combination of BC, OC and dust in snow, we did a sensitive test on two possible cases that the mixing ratios of BC, OC and Fe are 100 (15) ng g^{-1}, 1000 (150) ng g^{-1} and 50 (50) ng g^{-1} with the fractional absorption of 42% (34%), 54% (43%) and 4% (23%) based on our filed measurements. We estimated the relative uncertainty of the attributed absorption assuming the AAEs of BC, OC and Fe are 1.1±0.3, 6±2 and 3±1 (Doherty et al., 2010; Lack and Langridge, 2013) instead of 1.1, 6 and 3. As shown in Figure S1, the relative uncertainties of BC and OC are from -53% to 29% and -25% to 43%, respectively, which mainly resulted from the variations of AAEs of OC and BC (left panel). The variation of AAEs of Fe has a slight effect on the light absorption. For Fe, the relative uncertainty is from -18% to 22% based on the variation of AAEs. In case 2 (right panel), the fractional absorption of Fe is much more important compared with that in case 1. The relative uncertainties of BC and OC increased and range from -65% to 35% and -40% to 61%, which highlight the varied AAEs of Fe in uncertainty analysis. The analysis indicates that the changes of AAEs of Fe on uncertainty estimates are dependent on the fractional absorption of Fe.

3.4 PMF results

3.4.1 PMF model optimization

The concentrations of the components (chemical and optical constituents) and the associated uncertainty datasets were used to run the PMF 5.0 model. General speaking, three to seven factors, twelve to thirty components and seven or more random seeds were applied with an objective step-by-step methodology in the PMF model to obtain the best solution in accordance with stability, accuracy, performance, and geochemical likeliness. This methodology is a multistep procedure. Firstly, all of the available components are included. Additional adjustments of the selected input components, numbers of factors and random seeds are dependent on an iterative process. We indicate that the choice of uncertainties could lead an important effect on PMF results. Then, we examined several tests for the uncertainties calculations which includes: (1) combining the detection limit (twice of the standard deviation of the blank samples) and the coefficient of variation (standard deviation of repeated analysis divided by mean value of the repeated analysis), which have been performed by Anttila et al. (1995) and Gianini et al. (2012); (2) the uncertainty datasets were calculated by considering the relative uncertainties of the concentration of each component (Waked et al., 2014). We also considered the results of the bootstraps and examinations of the residuals. The ability of the PMF model to replicate experimental concentrations, especially for components regarded as markers of the specific emission sources, is one of the primary principles applied to assess the permanence of the results at each step. More details in PMF model optimization can be found in Waked et al. (2014) and Belis et al. (2014).

We used C_{BC}^{max} to estimate the fractional contributions to the 650-700-nm particulate absorption by all of the potential emission sources based on two reliable reasons: (1) C_{BC}^{max} represents the mass of BC, assuming all of the particulate light absorption (650-700 nm) is related to BC; (2) C_{BC}^{max} is only calculated based on the assumed MAC of BC; therefore, the errors of C_{BC}^{max} were the lowest among the studied variables. The chemical components were SO_4^{2-}, NO_3^-, Cl^-, F^-, Na^+, K^+, NH_4^+, $K_{Biosmoke}$, Al, Fe, Mn, Cu, Cr and Ba. Finally, a set of high uncertainty datasets was used in this study. For example, the relative uncertainty was 40% for C_{BC}^{max}, Na^+, K^+ and Al, 50 % for SO_4^{2-}, NO_3^- and $K_{Biosmoke}$, which was comparable with that used in other studies of the spatial variations (Hegg et al., 2009, 2010; Zhang et al., 2013a; Doherty et al., 2014). All these components were described from weak to strong in the PMF on account of their signal-to-noise ratio and the effect on tracing emission sources. The results indicated that the NO_3^-, NH_4^+, Cl^-, F^-, Cu and Cr were categorized as "weak". Therefore, the optimal number of factors/sources was four based on the robust and theoretical Q values (Hegg et al., 2009, 2010). However, three-factor provided more physically reasonable results and the most easily identifiable sources, which was consistent with studies of snow in northeastern China (Zhang et al., 2013a) and North America (Doherty et al., 2014). The diagnostic regression R^2 value for C_{BC}^{max} with this three-factor solution was considerably high (0.87). Hence, we indicated that the three-factor solution was the best choice in this study.

3.4.2 PMF source profile

Figure 5 shows the source profile, including the calculated mass concentrations (lines) and the percent of components apportioned to each factor (dots) for the three-factor solution. The first factor (top panel) was obviously characterized by high loadings of SO_4^{2-}, NO_3^-, Cl^-, and NH_4^+. SO_4^{2-} and NO_3^- are well-known markers for the burning of fossil fuel, such as coal and oil (e.g., Xie et al., 2008; Oh et al., 2011; Zhang et al., 2013b). Cl^- is usually regarded as an important component of sea salt but also a product of industrial emission (Kulkarni, 2009; Dall'Osto et al., 2013) and coal combustion (Hailin et al., 2008). Furthermore, the molar ratio of Cl^- to Na^+ was clearly larger than that of sea salt by a factor of > 2, which implied another source in addition to sea salt. Additionally, NH_4^+ is a recognized marker of coal combustion. However, the ratio of C_{BC}^{max} to SO_4^{2-} was low (0.04) and close to the values in pollution sources as reported by Hegg et al. (2009). Therefore, we considered the first factor an industrial pollution source. The second factor (middle panel) presented substantial loadings of Na^+, K^+, and $K_{Biosmoke}$. However, chemical analyses are not available for certain organic matter, including levoglucosan, succinate, oxalate, and formate, which generally indicate biomass burning. K^+ and $K_{Biosmoke}$ are markers for biomass burning emissions and were highly loaded for this factor. In particular, $K_{Biosmoke}$, which was calculated as the biosmoke fraction of K, was representative (Zhang et al., 2013a). Compared with the first factor, the molar ratio of Cl^- to Na^+ was smaller than 1, which indicates that Na^+ was also a potential product of emission sources in addition to sea salt, such as biomass burning (Oh et al., 2011). However, the ratio of C_{BC}^{max} to SO_4^{2-} was relatively high compared with that of the previously

identified industrial pollution sources and close to the ratio for a biomass burning source as reported by Doherty et al. (2014). Therefore, we interpreted the second factor as a biomass burning source. The third factor (bottom panel) accounted for over 50% Al, Cr, Fe, Cu, and Ba in the samples. Al and Fe are well-known crustal constituents, and they are usually used to determine the mass of soil dust. The mass ratio of Fe to Al (0.36) was close to the value in the continental crust (0.40) (Wedepohl, 1995). Furthermore, the enrichment factors (EFs) of the trace elements, including Cr, Cu, and Ba, were < 5 at many sample sites, which indicates that these elements may have originated from a crustal source (Zhang et al., 2013b). Hence, we can interpret the third factor as a soil dust source.

3.4.3 Source attribution in snow

Figure 6 shows the mean normalized contributions from each source to the individual receptor site. The industrial pollution source with a 31% C_{BC}^{max} dominated the contributions to the sites in Region 3. In particular, the mean normalized contributions were > 5 at sites 60 and 84, which was consistent with the abundant loadings of SO_4^{2-} and NO_3^-. The results were not surprising because substantial industrial activity occurs in this region. However, the contributions from the biomass burning source with the highest C_{BC}^{max} (53%) were more geographically dispersed and relatively evenly distributed across Regions 1, 2, and 4. At sites 53 and 67, the contributions were significantly large, which were likely caused by the concentrations of $K_{Biosmoke}$, which were over 500 ng g^{-1} and much higher than those at the other sites. Indeed, biomass burning, such as biofuel combustion for heating, in winter and early spring in

northwestern China is normally prevalent (Pu et al., 2015). Unsurprisingly, a soil dust

source, which was characterized by the highest loadings of Al and Fe, was mainly

associated with the sites in Qinghai (Region 1), although the contributions were

obvious at certain sites in Xinjiang, especially the sites in Region 5, which was

5   partially because these sites were located on hills with scarce plants, and wind may

have blown local soil dust onto the snow.

The fractional contributions from the three sources to the 650-700-nm particulate

absorption at each individual receptor site are shown in Figure 7. The average

regional contributions are shown in Table 5. The most remarkable feature of the

10   source attributions is the differences observed by region. Biomass burning was the

primary source in Region 1 (in Qinghai) and in Regions 2 and 4 (in Xinjiang), and it

presented average regional contributions of 59%, 60%, and 67%, respectively.

Although high dust mass was present in the snow samples from Region 1, this source

attribution was reasonable because the C_{BC}^{max} from the biomass burning sources was

15   much larger than that from the soil dust sources by a factor of > 3 (Figure 6). In

particular, biomass burning in Qinghai is prevalent, especially during winter (Yan et

al., 2006). In Region 1, soil dust accounted for 29% of the particulate absorption,

which was less than the contribution from the biomass burning sources but more

significant compared with the contributions from soil dust in the other regions. In

20   Regions 2 and 4, most of the sample sites were located on mountains and far from

industrial areas; therefore, dominant absorption by biomass burning sources was not

anomalous. The only exception was site 58, which was dominated by industrial

pollution sources, and this result was likely because of its shorter distance from cities and lower elevation. In Region 3, all of the sample sites were located near cities and suffered from anthropogenic emissions; therefore, industrial pollution was the primary source and presented a contribution of 58%. In Region 5, the primary source differed between sites. Absorption was dominated by biomass burning sources at sites 73 and 78, by industrial pollution sources at sites 72, 74, and 76, and by soil dust sources at sites 75 and 77. More complex topography and emission sources could partly explain these findings.

The PMF results in Qinghai in this study were not comparable well with those by Zhang et al. (2013a), who indicated that soil dust was the dominant source of ILAPs. However, the discrepancy could be concluded as (1) the receptor sites between two field campaigns were really far; (2) the chemical components inputs were different (e.g. K^+ and $K_{Biosmoke}$ instead of levoglucosan as the markers for biomass burning emissions); (3) the variables that characterized the particulate light absorption in the PMF analysis were inconsistent that we used C_{BC}^{max} instead of ILAPs to estimate the fractional contributions to the 650-700-nm particulate absorption. Hence, additional sample sites and more complete and advanced analyses of ILAPs and chemical components inputs to the PMF model are necessary to obtain more representative source analysis results.

3.4.4 Altitude gradients of BC mass

Ye et al. (2012) performed a preliminary study on the same field campaign and found that the snow BC mixing ratios, which were based on visual estimates, were

negatively correlated with the altitudes of the sample sites in Xinjiang. In our study, the C_{BC}^{est} and C_{BC}^{max} values from the ISSW presented a similar trend (Figure 8a and b). Thus, altitude is an important influencing factor for BC mixing ratios and particulate absorption. Additionally, the C_{BC}^{max} value simulated by the PMF model decreased

5   steadily with altitude, although this trend was not as obvious as that for the measured C_{BC}^{est} and C_{BC}^{max}. Therefore, we can explore the cause of altitude gradients for the BC mass based on the PMF three-factor solution. Figure 9 shows the scaled contributions of each source, which was obtained by multiplying the simulated contributions by the ratio of measured to calculated C_{BC}^{max}, as a function of altitude. We note that the snow

10   samples with scaled contributions larger than 3 were removed due to heavy polluted snow samples (Ye et al., 2012). Clearly, the contributions from industrial pollution sources presented a decreasing trend with altitude and was highly related to the altitude, while the biomass burning and soil dust only showed weak correlations. Thus, the altitude gradients of the contributions from industrial pollution likely caused the

15   altitude gradients of the BC mass.

3.5 Mass contribution of the chemical components

In addition to performing a PMF analysis, the chemical components must be evaluated to examine the potential emission sources. As shown in Figure 10a, the median mass concentrations of chemicals in the different regions were 6.0 μg g^{-1}

20   (Region 1), 5.0 μg g^{-1} (Region 2), 7.0 μg g^{-1} (Region 3), 5.0 μg g^{-1} (Region 4), and 4.6 μg g^{-1} (Region 5). At sites 60 and 84, the mass concentrations were > 20 μg g^{-1}, which were primarily contributed by SO_4^{2-} and NO_3^-. Regionally, the chemical components

were dominated by MD (30.5%) and OC (29.5%) in Region 1, MD (21.1%) and SO_4^{2-}

(20.2%) in Region 2, SO_4^{2-} (21.5%) and NO_3^- (29.2%) in Region 3, SO_4^{2-} (17.9%)

and NO_3^- (33.7%) in Region 4, and MD (29.5%) and NO_3^- (27.5%) in Region 5

(Figure 10b). These results indicated that soil dust sources greatly contributed to the

5   chemical components in Region 1, whereas industrial pollution was the predominant

source in Regions 3 and 4. In the other regions, the fractional contributions from

different sources to the mass concentrations were comparable. The mass contribution

was not proportional to the absorption contribution because of the different ILAPs

loadings of emission sources. For example, although SO_4^{2-} and NO_3^- are major

10   components, the 650-700-nm particulate absorption in Region 4 was dominated by a

biomass burning source. BC is regarded as an important light-absorbing particle, and

it ranged from 0.2 to 4.8% in mass at all sites, with an average of 1.3%, which is

smaller than that (2.4-5.1%) in urban areas in China (Huang et al., 2014). $K_{Biosmoke}$ is a

good indicator of biomass burning, and it ranged from 0.4 to 7.8% and presented the

15   largest regional average fractional contribution (3.0%) in Region 2. Wang et al. (2016)

reported comparable values of 1.3-5.1% in the snow in northeastern China.

3.6 Comparative analysis of chemical components

Bond et al. (2004) indicated that the OC:BC ratio of the emissions from fossil fuel

burning is lower than that from biomass or biofuel burning; therefore, we may

20   qualitatively examine the primary emission sources based on this theory. In this work,

the regional average ratios of OC to BC were 20.9, 6.12, 3.99, 6.71, and 7.28 (Figure

11a). The smallest value in Region 3 was similar to those observed in Beijing (Zhang

et al., 2013b). The similar ratios in Regions 2, 4, and 5 were close to that of savanna and grassland regions as reported by Andreae and Merlet (2001). The results suggested the relative dominance of an industrial pollution source in Region 3 and a biomass burning source in other regions in Xinjiang. This pattern was similar to that of the source apportionment analysis by the PMF model. The largest value in Region 1 in Qinghai implied a primary contribution to OC from soil dust.

Sources of nitrate are considerably more varied than the sources of sulfate (Arimoto et al., 1996). For NO_3^-, the largest source is fossil fuel combustion. Biomass burning is regarded as another main source, which was determined according to the analysis of Logan. Additionally, microbial activity in soil is a potential source of nitrate. However, SO_4^{2-} is mainly a product of burning coal. Thus, we can compare the correlation between NO_3^- and SO_4^{2-} to explore the variety of emission sources. As shown in Figure 11b, the average regional ratio of NO_3^- to SO_4^{2-} in Region 1 was 0.49, which was lower than that in the other regions. The concentrations and correlation coefficients of NO_3^- and SO_4^{2-} were both the lowest in Region 1, which indicates limited emissions from an industrial pollution source. In Xinjiang, the ratios mostly ranged from 1 to 1.5, and the high correlation coefficient in Region 5 was associated with similar industrial pollution sources, whereas the low correlation coefficients in Regions 2-4 may have been related to complicated industrial pollution sources.

A comparison between cations and anions is shown in Figure 11c. Generally, the correlation coefficients were all significant at the 5% level. A large anion charge deficit was observed in Region 1, which presented an average regional ratio of 2.93,

which was likely caused by the absence of detected CO_3^{2-} and HCO_3^-. Carbonates (e.g., $CaCO_3$ and $MgCO_3$) are often abundant in dust, which was observed in the Central Himalayan Glacier (Xu et al., 2013), and account for the largest contribution from soil dust to the mass concentration. However, the average ratios in the sample snow in Xinjiang were generally uniform and ranged from 0.7-1.2, which suggests an adequate charge balance. Overall, the concentrations of inorganic ions in the snow samples were lower than those in the rainwater in urban sites in China (Wang and Han, 2011) but larger than previous measurements in the Himalayas (Thompson et al., 2000; Xu et al., 2013).

4 Conclusions

A large field campaign was conducted in northwestern China from January to February 2012. The cleanest snow of this campaign was found in the northeast of Xinjiang along the border of China, and the lowest C_{BC}^{est} values were approximately 5 ng g^{-1}. The highest C_{BC}^{est} value was approximately 450 ng g^{-1} at site 60, which was located in proximity to industrial cities. In Qinghai, OC dominated the 450-nm absorption, and the fractional contribution reached approximately 70%. Although dust accounted for the main portion of the particulate mass, the fractional contribution from Fe to absorption (approximately 5%) was not significant. In Xinjiang, the fractions of absorption from BC (45%) and OC (50%) were comparable, and the effect of Fe was limited. In the Tianshan Mountains (Regions 2 and 3), the $\mathring{A}_{tot}$ and f_{nonBC}^{est} values presented vertical changes from the subsurface to surface snow, which indicates a probable shift in emission sources as winter progressed.

A three-factor solution (industrial pollution, biomass burning and soil dust) was used to explore the fractional contributions from the different sources within the particulate absorption range from 650-700 nm based on a source apportionment analysis with the PMF model. In Qinghai, biomass burning was the primary source (59%), and soil dust accounted for 29% of the particulate absorption despite its high mass contribution. In Xinjiang, the source attributions varied by region. In Regions 2 and 4, most of the sample sites were located on mountains and far from industrial areas, and biomass burning sources were dominant and accounted for 60% and 67% of the contributions, respectively. In Region 3, absorption was dominated by an industrial pollution source (58%) because of the shorter distance from cities and lower elevations. In Region 5, the topography and emission sources were more complex, and the primary sources differed between sites. However, the BC mixing ratios showed a negative correlation with altitude in Xinjiang, which likely resulted from gradient variations in the contributions of industrial pollution sources. An evaluation indicated that the predominant source of chemical components was soil dust in Region 1, while industrial pollution in Regions 3 and 4. The mass of BC, which is regarded as an important light-absorbing particle, ranged from 0.2 to 4.8% and presented an average of 1.3%. A comparison between OC and BC suggested the relative dominance of an industrial pollution source in Region 3 and a biomass burning source in other regions in Xinjiang.

5 Data availability

All data sets and codes used to produce this study can be obtained by contacting Xin Wang (wxin@lzu.edu.cn). The elevation data used in this study is available: http://rda.ucar.edu/datasets/ds759.3/#!access.

Competing interests. The authors declare that they have no conflict of interest.

Acknowledgements. This research was supported by the Foundation for Innovative Research Groups of the National Science Foundation of China (41521004), the National Science Foundation of China under Grants 41522505, and the Fundamental Research Funds for the Central Universities (lzujbky-2015-k01, lzujbky-2016-k06 and lzujbky-2015-3). We thank Jinsen Shi, Hao Ye of Lanzhou University and Rudong Zhang of Nanjing University for their assistance in field sampling.

Table 1. Variables derived by using the ISSW spectrophotometer.

Symbols	Description of variables
C_{BC}^{max}	Maximum BC is the mass of BC per mass of snow, if all particulate light absorption (650–700nm) is due to BC.
C_{BC}^{est}	Estimated BC is the estimated true mass of BC per mass of snow, derived by separating the spectrally resolved total light absorption.
C_{BC}^{equiv}	Equivalent BC is the amount of BC that would need to be present in the snow to account for the wavelength-integrated (300–750nm) total light absorption of down-welling solar radiation by all particulate constituents.
$\mathring{A}_{tot}$	Absorption Ångström exponent is calculated between 450 and 600nm, for all particulate deposited on the filter.
f_{nonBC}^{est}	Fraction of light absorption by non-BC ILAPs, is the absorption by non-BC particulate constituents, weighted by the down-welling solar flux, then spectrally integrated from 300 to 750nm.

Table 2. Statistics of the seasonal snow variables measured using an ISSW for each site.

| Site | Layer | Latitude | Longitude | Average snow depth | Sample depth (cm) | | C_{BC}^{equiv} | C_{BC}^{max} | C_{BC}^{est} | f_{non-BC}^{est} | $Å_{tot}$ |
		(N)	(E)	(cm)	Top	Bottom	(ng g^{-1})	(ng g^{-1})	(ng g^{-1})	(%)	
47	1	35.54	99.49	2.5	0	5	480	242	148(—,235)	73(55,—)	4.58
	2				5	10	487	266	175(—,262)	64(46,—)	4.02
	3				10	15	1094	548	358(—,556)	67(49,—)	4.30
	4				15	20	314	200	156(29,217)	52(33,—)	3.55
48	1	34.85	98.13	4.5	0	1	334	196	152(65,222)	58(37,—)	3.87
	2				2	4	237	129	83(—,134)	65(43,—)	4.09
49	1	35.22	98.95	10	0	1	317	160	118(—,179)	66(47,—)	4.36
	2				2	7	—	—	—(—,—)	—(—,—)	—
	3				11	16	315	156	102(—,164)	64(42,—)	4.38
	4				16	25	203	90	53(—,84)	74(59,—)	4.20
50	1	34.80	99.05	—	0	2	165	66	28(—,54)	83(67,—)	4.57
	2				2	7	—	—	—(—,—)	—(—,—)	—
	3				7	12	—	—	—(—,—)	—(—,—)	—
	4				12	20	202	105	63(—,107)	69(47,—)	4.37
51a	1	33.89	99.80	5	0	4	318	183	135(19,193)	55(36,—)	3.91
	2				4	6	—	—	—(—,—)	—(—,—)	—
51b	1	33.89	99.80	5	0	1	389	148	77(—,125)	80(68,—)	4.27
52	1	34.92	100.89	3.5	0	1	144	65	33(—,56)	77(61,—)	4.09
	2				2	4	—	—	—(—,—)	—(—,—)	—
53	1	43.07	86.81	7	0	8	595	427	334(201,48)	44(19,66)	2.50
	2				8	16	489	354	264(173,40)	46(18,65)	2.46
	3				16	26	522	376	254(177,42)	51(20,67)	2.51
54	1	43.08	85.82	25	0	2	36	18	7(—,13)	81(65,—)	4.48
	2				2	9	25	15	6(—,10)	75(58,—)	4.15

Site	Layer	Latitude (N)	Longitude (E)	Average snow depth (cm)	Sample depth (cm) Top	Sample depth (cm) Bottom	C_{BC}^{equiv} (ng g^{-1})	C_{BC}^{max} (ng g^{-1})	C_{BC}^{est} (ng g^{-1})	f_{non-BC}^{est} (%)	Å_{tot}
	3				12	17	111	86	68(25,87)	39(22,78)	2.91
55	1	43.51	83.54	25	0	4	146	110	96(52,122)	32(30,63)	2.57
	2				4	8	111	111	97(61,120)	13(7,45)	2.22
56	1	43.66	82.75	24	0	4	90	61	45(16,59)	50(34,82)	2.92
	2				4	8	162	114	99(47,126)	43(27,74)	2.72
	3				8	12	—	—	—(—,—)	—(—,—)	—
57	1	43.64	82.11	15	0	4	151	124	106(57,133)	40(25,58)	2.52
	2				4	9	106	78	62(34,77)	42(27,68)	2.42
	3				9	13	—	—	—(—,—)	—(—,—)	—
58	1	43.52	81.13	37	0	4	37	26	10(1,21)	73(43,97)	3.38
	2				4	8	50	35	18(8,30)	64(38,83)	2.91
	3				8	13	118	83	63(42,85)	47(29,64)	2.25
	4				13	18	61	32	15(5,28)	79(53,—)	3.51
	5				18	23	70	42	25(13,39)	66(43,84)	2.82
	6				25	30	141	133	117(85,147)	17(5,40)	1.96
59	1	44.49	81.15	60	0	5	116	51	24(—,38)	80(68,—)	4.29
	2				5	10	109	37	16(—,27)	85(75,—)	4.41
	3				10	15	195	99	67(15,91)	65(53,98)	3.45
	4				15	20	175	98	73(23,95)	58(46,87)	2.99
	5				20	28	184	97	71(19,93)	62(50,90)	3.08
	6				28	36	204	102	67(—,93)	67(54,—)	3.60
60	1	44.96	82.63	5	0	2	696	542	473(352,58)	32(17,49)	1.84
	2				2	5	—	—	—(—,—)	—(—,—)	—
61	1	44.38	83.09	23	0	3	192	113	83(37,107)	57(45,81)	2.73
	2				3	6	286	197	156(56,200)	45(30,80)	2.88

Site	Layer	Latitude	Longitude	Average snow depth	Sample depth (cm)		C_{BC}^{equiv}	C_{BC}^{max}	C_{BC}^{est}	$f_{non\text{-}BC}^{est}$	$\mathring{A}_{tot}$
		(N)	(E)	(cm)	Top	Bottom	(ng g^{-1})	(ng g^{-1})	(ng g^{-1})	(%)	
	3				6	15	260	144	110(47,141)	58(46,82)	2.74
	4				15	19	94	69	45(18,60)	52(36,81)	2.85
62	1	44.57	83.96	8	0	1	105	71	50(26,64)	53(38,77)	2.58
	2				1	4	144	80	56(24,74)	61(49,84)	2.79
63	1	45.58	84.29	10	0	1	169	109	82(40,108)	52(37,77)	2.69
64	1	46.68	83.54	25	0	2	325	199	152(38,205)	51(34,94)	3.41
	2				2	6	269	120	84(11,114)	69(58,96)	3.31
	3				6	10	893	363	240(—,336)	73(63,—)	3.75
	4				10	15	268	125	75(—,106)	72(61,—)	3.61
65	1	46.49	85.04	4	0	2	156	108	83(33,106)	46(31,79)	2.85
66	1	46.88	85.92	15	0	5	57	40	24(1,33)	58(42,—)	3.48
	2				5	10	134	98	75(22,96)	46(30,85)	3.06
67	1	47.26	86.71	7	0	4	611	446	386(379,48)	38(22,72)	2.73
	2				4	10	298	234	192(96,243)	38(21,71)	2.68
	3				10	16	256	195	140(48,183)	45(28,81)	2.93
68	1	48.15	86.56	32	0	5	140	120	87(46,112)	38(20,67)	2.52
	2				5	10	84	70	46(21,62)	45(26,75)	2.72
	3				10	15	104	82	58(26,77)	44(26,75)	2.74
	4				15	20	20	15	6(1,12)	70(40,95)	3.33
69	1	47.86	86.29	4	0	1	320	264	208(137,26)	36(19,59)	2.22
	2				1	4	191	155	112(64,147)	42(23,67)	2.45
70	1	48.33	87.13	70	0	3	39	24	12(—,18)	68(53,—)	3.93
	2				3	8	31	21	13(0,17)	59(44,99)	3.46
	3				10	15	42	29	18(2,24)	57(42,96)	3.37
	4				15	20	9	6	3(—,4)	68(51,—)	3.69

Site	Layer	Latitude (N)	Longitude (E)	Average snow depth (cm)	Sample depth (cm) Top	Sample depth (cm) Bottom	C_{BC}^{equiv} (ng g^{-1})	C_{BC}^{max} (ng g^{-1})	C_{BC}^{est} (ng g^{-1})	f_{non-BC}^{est} (%)	$Å_{tot}$
	5				20	25	18	13	8(1,10)	57(41,94)	3.30
	6				25	30	29	25	16(7,21)	43(27,75)	2.74
	7				30	35	21	17	11(3,14)	50(34,85)	3.03
	8				35	40	36	28	19(6,24)	48(32,83)	2.97
71	1	48.07	87.03	40	0	5	96	76	52(21,69)	45(29,78)	2.81
	2				5	10	88	70	48(20,63)	45(28,78)	2.81
	3				13	18	30	23	13(2,19)	58(39,92)	3.26
	4				20	25	33	27	17(7,23)	50(30,80)	2.87
	5				25	30	128	101	85(60,104)	33(18,53)	1.96
72	1	47.79	87.56	20	0	3	272	213	135(45,185)	50(32,83)	2.97
	2				3	8	167	135	90(47,125)	47(26,72)	2.64
	3				8	12	88	71	40(18,62)	56(30,80)	2.87
73	1	47.55	88.61	41	0	4	101	73	50(15,66)	51(35,86)	3.04
	2				4	9	108	79	56(21,73)	49(33,81)	2.88
	3				10	15	42	30	17(2,24)	61(43,98)	3.43
	4				15	20	45	34	21(5,28)	55(37,90)	3.16
	5				20	26	91	73	52(24,66)	43(27,74)	2.69
	6				26	32	77	63	44(21,57)	43(26,73)	2.67
74	1	47.63	88.40	34	0	4	174	139	115(73,142)	34(30,59)	2.24
	2				4	9	129	95	70(35,90)	46(31,73)	2.59
	3				10	15	76	61	41(17,54)	46(28,77)	2.78
	4				15	21	73	58	39(16,51)	47(30,78)	2.82
	5				21	25	83	67	46(21,60)	44(27,75)	2.70
75	1	47.58	88.78	40	0	5	45	29	10(—,23)	80(50,—)	3.81
	2				5	10	38	25	7(—,19)	82(50,—)	3.74

Site	Layer	Latitude (N)	Longitude (E)	Average snow depth (cm)	Sample depth (cm) Top	Sample depth (cm) Bottom	C_{BC}^{equiv} (ng g^{-1})	C_{BC}^{max} (ng g^{-1})	C_{BC}^{est} (ng g^{-1})	f_{non-BC}^{est} (%)	Å_{tot}
	3				10	15	—	—	—(—,—)	—(—,—)	—
	4				15	22	22	16	4(1,13)	84(40,94)	3.29
	5				24	29	78	53	33(18,49)	58(36,77)	2.66
	6				30	35	45	35	18(8,30)	61(32,81)	2.90
	7				35	40	29	21	7(2,17)	77(39,93)	3.28
	8				40	45	27	19	5(1,15)	81(42,97)	3.40
76	1	47.17	88.70	26	0	2	315	218	144(77,202)	54(35,76)	2.63
	2				2	6	229	168	113(78,159)	51(30,67)	2.30
	3				6	11	210	173	110(63,158)	48(25,70)	2.56
	4				11	16	93	74	32(15,62)	66(34,84)	2.99
77	1	47.27	89.97	45	0	4	53	39	17(5,33)	68(39,91)	3.21
	2				5	10	40	29	11(3,24)	74(40,92)	3.23
	3				10	15	20	14	1(0,11)	97(44,99)	3.46
	4				15	20	—	—	—(—,—)	—(—,—)	—
	5				20	25	21	16	2(1,12)	91(41,94)	3.29
	6				25	30	19	14	1(1,11)	96(44,98)	3.44
	7				30	35	17	14	1(1,11)	96(40,92)	3.22
	8				35	40	—	—	—(—,—)	—(—,—)	—
	9				40	45	—	—	—(—,—)	—(—,—)	—
78	1	46.85	90.32	35	0	2	147	75	44(3,63)	71(57,—)	3.73
	2				2	7	39	24	10(—,17)	75(56,—)	4.01
	3				7	12	23	16	7(—,12)	71(47,—)	3.60
	4				12	17	33	22	11(—,18)	67(46,—)	3.55
	5				17	22	13	10	4(—,7)	76(46,—)	3.55
	6				22	27	30	21	11(0,17)	65(44,98)	3.45

Site	Layer	Latitude (N)	Longitude (E)	Average snow depth (cm)	Sample depth (cm) Top	Sample depth (cm) Bottom	C_{BC}^{equiv} (ng g^{-1})	C_{BC}^{max} (ng g^{-1})	C_{BC}^{est} (ng g^{-1})	f_{non-BC}^{est} (%)	$Å_{tot}$
79	1	43.53	89.74	30	0	6	78	41	21(—,33)	74(58,—)	4.04
	2				6	11	62	38	20(—,30)	67(50,—)	3.75
	3				11	18	68	41	21(—,32)	69(53,—)	3.89
	4				18	24	84	50	28(—,40)	67(52,—)	3.71
	5				24	30	83	54	32(4,45)	61(45,95)	3.33
	6				30	35	171	116	86(42,110)	49(35,75)	2.65
	7				35	40	165	99	66(21,87)	60(47,87)	2.98
80	1	44.10	87.49	18	0	3	176	109	67(29,95)	63(47,94)	3.28
	2				3	7	50	33	12(—,25)	76(51,—)	3.75
81	1	43.60	87.51	6	0	3	172	89	51(8,74)	71(57,—)	3.66
	2				3	6	189	89	53(1,76)	72(60,—)	3.50
82	1	44.09	84.80	13	0	5	48	24	9(—,15)	81(68,—)	4.66
	2				5	9	28	16	8(—,11)	73(59,—)	4.22
83	1	43.93	85.41	12	0	3	101	66	37(3,53)	64(48,—)	3.54
	2				3	7	48	31	14(—,23)	71(52,—)	3.81
	3				8	12	1087	841	619(336,76)	43(29,69)	2.44
84	1	43.93	86.76	25	0	2	489	372	250(127,34)	49(30,74)	2.63
	2				2	6	76	50	7(—,38)	91(49,—)	3.68

Table 3. Surface and subsurface snow sample average values within the five sample regions in Figure 1.

Regions	Layers	C_{BC}^{max}	C_{BC}^{est}	C_{BC}^{equiv}	$Å_{tot}$	f_{non-BC}^{est}
		(ng g^{-1})	(ng g^{-1})	(ng g^{-1})		(%)
1	surface	151±66	99±53	307±119	4.24±0.29	70±11
	subsurface	174±110	113±78	332±201	4.17±0.19	66±4
2	surface	108±126	81±102	160±171	3.27±0.80	59±19
	subsurface	119±96	89±69	170±134	2.86±0.49	49±16
3	surface	173±183	127±158	245±226	3.11±0.86	58±15
	subsurface	117±158	75±120	175±201	3.51±0.50	72±12
4	surface	160±141	126±124	218±192	2.99±0.56	48±11
	subsurface	114±77	82±56	178±157	2.96±0.36	51±10
5	surface	112±79	74±56	158±104	3.09±0.56	58±16
	subsurface	61±46	37±31	80±57	3.03±0.37	62±16

Table 4. Total snow water equivalent (SWE) and estimated total snowpack BC mass in a 1-cm^2 column of snow.

Site	Date sampled	Integrated SWE	Integrated BC	Snowpack average BC mixing ratio
	(2012)	(g cm^{-2})	(ng cm^{-2})	(ng g^{-1})
47	10 Jan	5.94	1212	204
48	11 Jan	0.51	54	106
49	11 Jan	3.77	—	74
50	1 Jan	1.56	—	57
51a	12 Jan	1.52	—	135
51b	12 Jan	0.14	11	77
52	13 Jan	0.14	—	33
53	31 Jan	9.18	2632	287
54	1 Feb	2.41	64	27
55	2 Feb	1.16	112	96
56	2 Feb	1.16	—	76
57	2 Feb	1.99	—	80
58	3 Feb	5.33	244	46
59	4 Feb	7.67	451	59
60	4 Feb	0.22	—	473
61	5 Feb	2.87	265	92
62	8 Feb	0.56	30	54
63	9 Feb	—	—	—
64	9 Feb	2.2	283	129
65	10 Feb	—	—	—
66	10 Feb	1.45	80	55
67	11 Feb	5.64	1320	234
68	11 Feb	2.9	128	44
69	11 Feb	—	—	—
70	12 Feb	7.9	99	13
71	12 Feb	5.15	226	44
72	14 Feb	1.74	138	80
73	14 Feb	5.96	236	40
74	14 Feb	4.16	235	56
75	17 Feb	7.64	—	12
76	18 Feb	2.68	230	86
77	19 Feb	6.1	—	4
78	20 Feb	5.07	53	10
79	21 Feb	7.05	282	40
80	23 Feb	0.91	32	35
81	23 Feb	1.02	53	52
82	24 Feb	0.97	8	8
83	24 Feb	1.43	343	240
84	25 Feb	0.66	58	88

Table 5. Average regional contributions to the 650-700-nm particulate absorption.

Regions	Industrial pollution (%)	Biomass burning (%)	Soil dust (%)
1	12	59	29
2	25	60	15
3	58	31	10
4	27	67	5
5	41	28	31
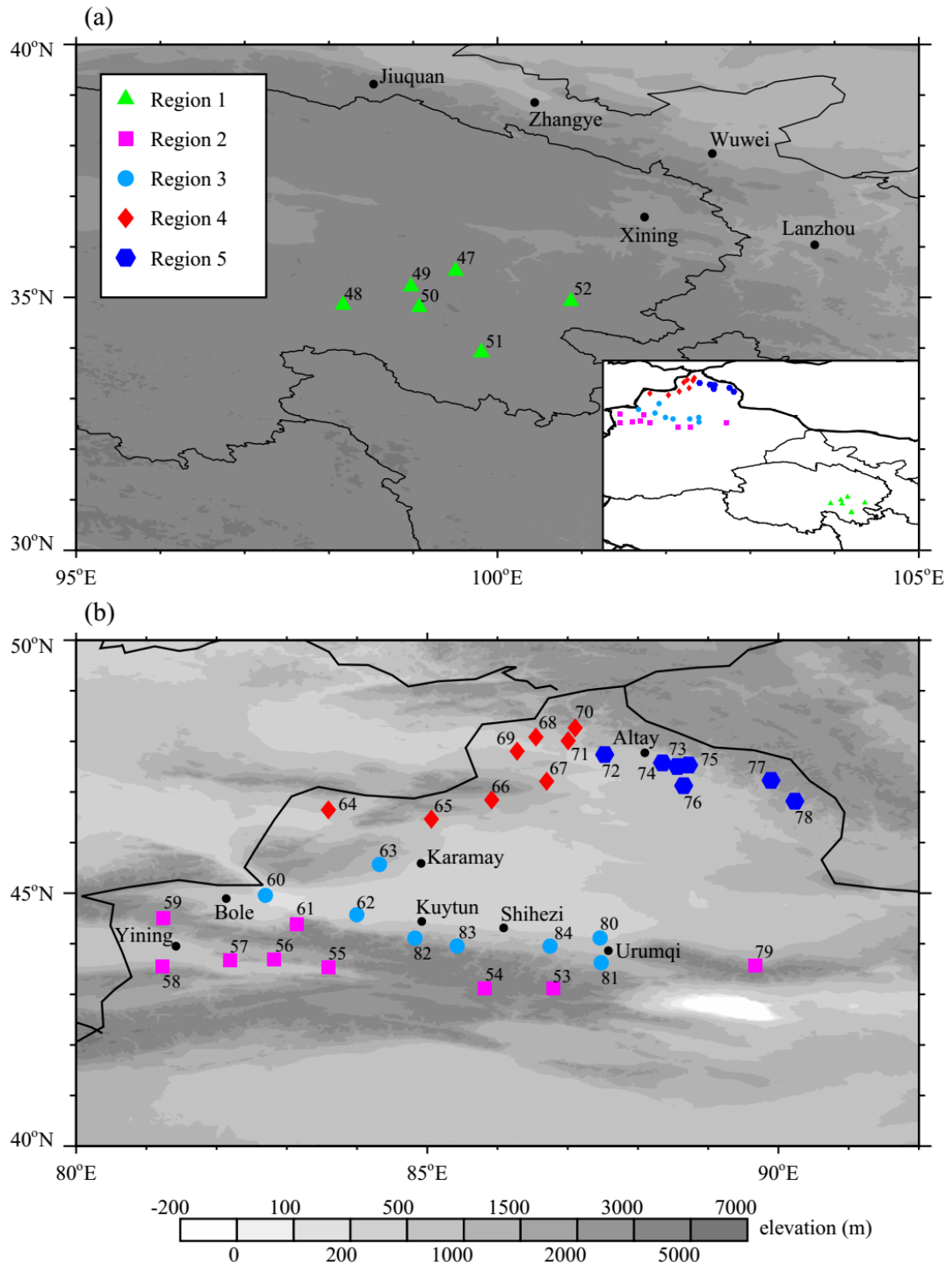
Fig. 1. Snow sampling locations, site numbers, and regional groupings in (a) Qinghai and (b) Xinjiang, black filled circle are the locations of main cities on the map.
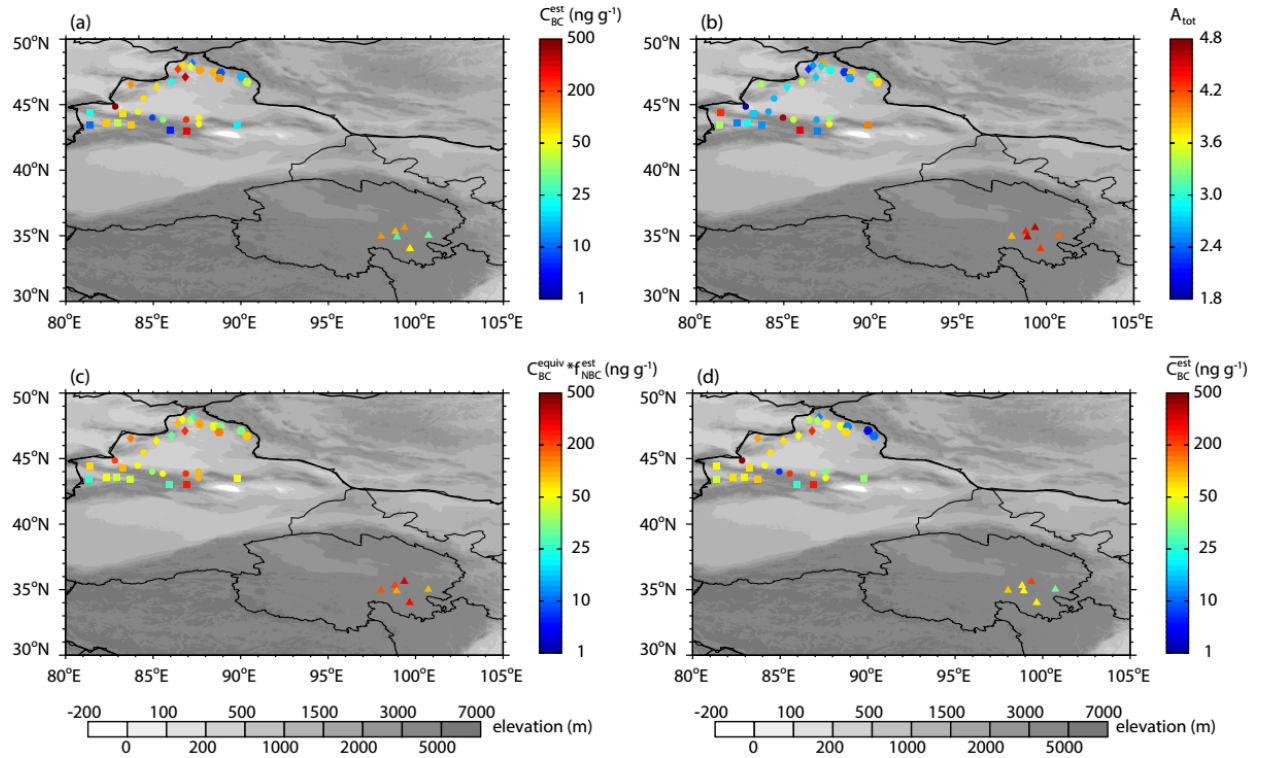
Fig. 2. (a) C_{BC}^{est} and (b) $Å_{tot}$ for the surface layer at each site, with symbols according to region (see Figure 1). (c) Estimated BC-equivalent mixing ratio (ng g^{-1}) required to explain the spectrally integrated (300–750 nm) absorption of sunlight by non-BC components in snow. (d) Estimated average snow BC mixing ratio, $\overline{C_{BC}^{est}}$, which was calculated by integrating the snow water content and BC mass over the entire snowpack (see Table 4).
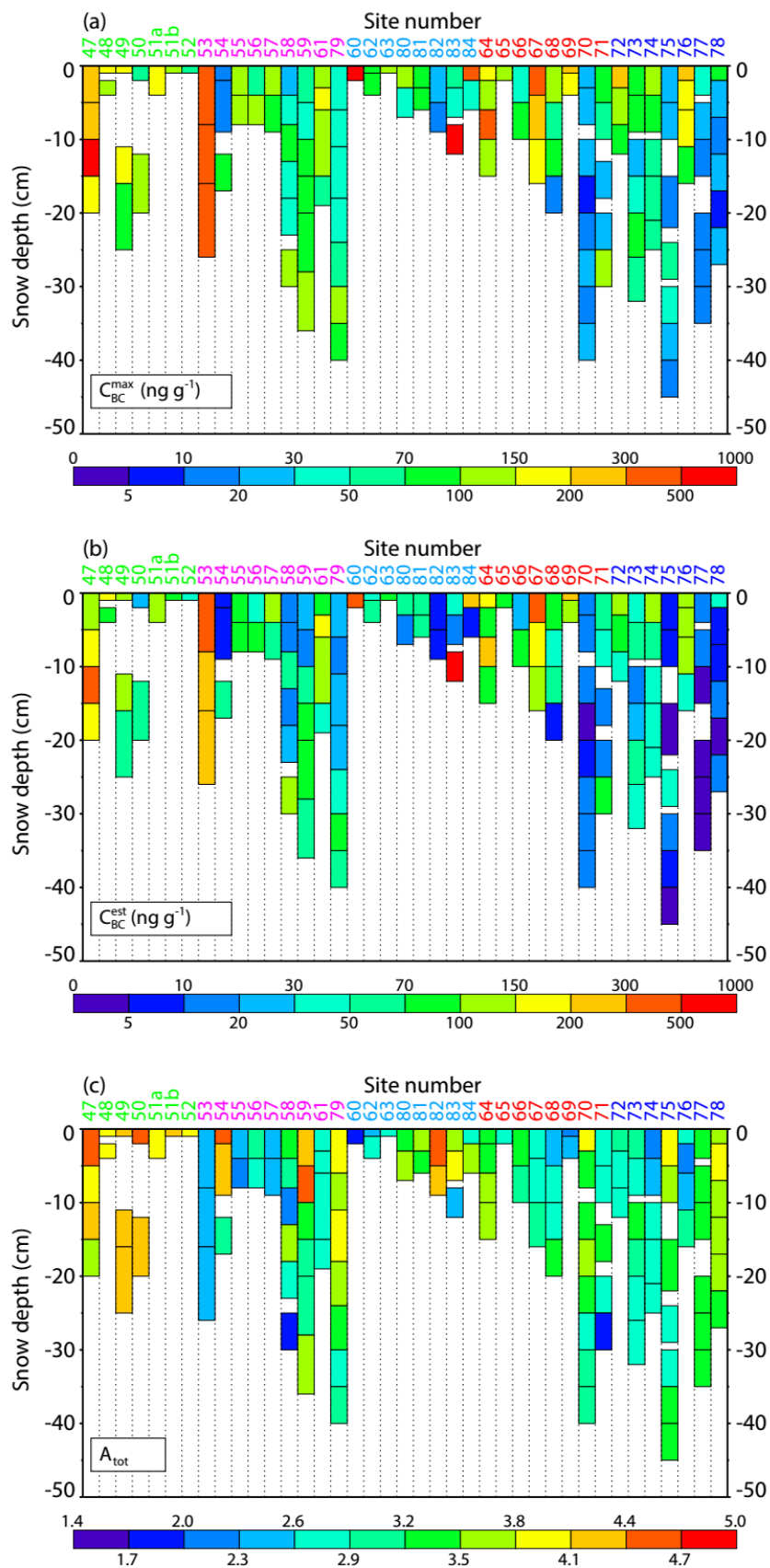
Fig. 3. Vertical profiles of the (a) C_{BC}^{max}, (b) C_{BC}^{est}, and (c) $Å_{tot}$ at each sampling site.
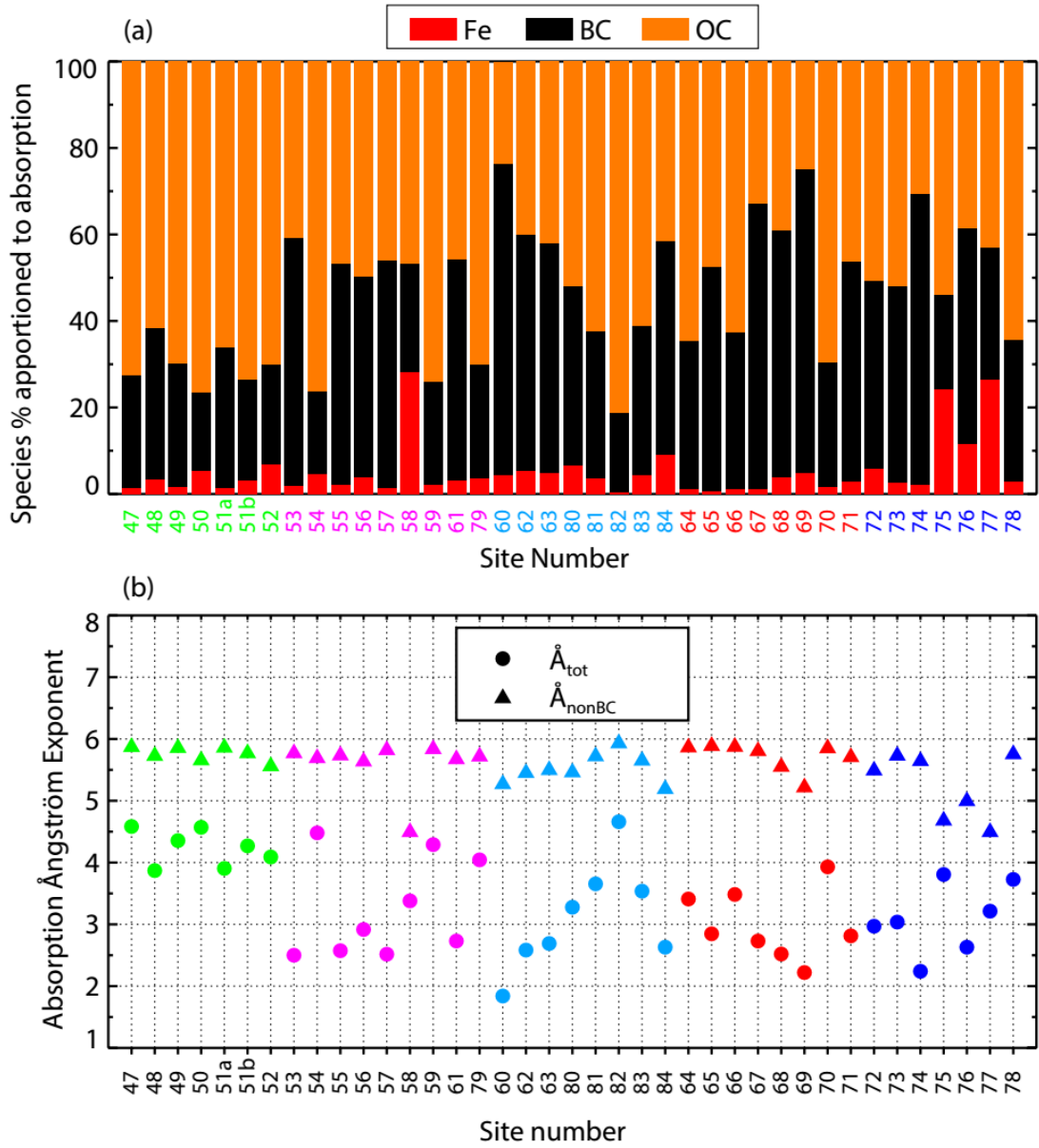
Fig. 4. (a) Relative contributions from the BC, OC, and Fe oxides to the total absorption optical depth for the surface snow samples. (b) $Å_{tot}$ and $Å_{nonBC}$ for the surface snow samples.
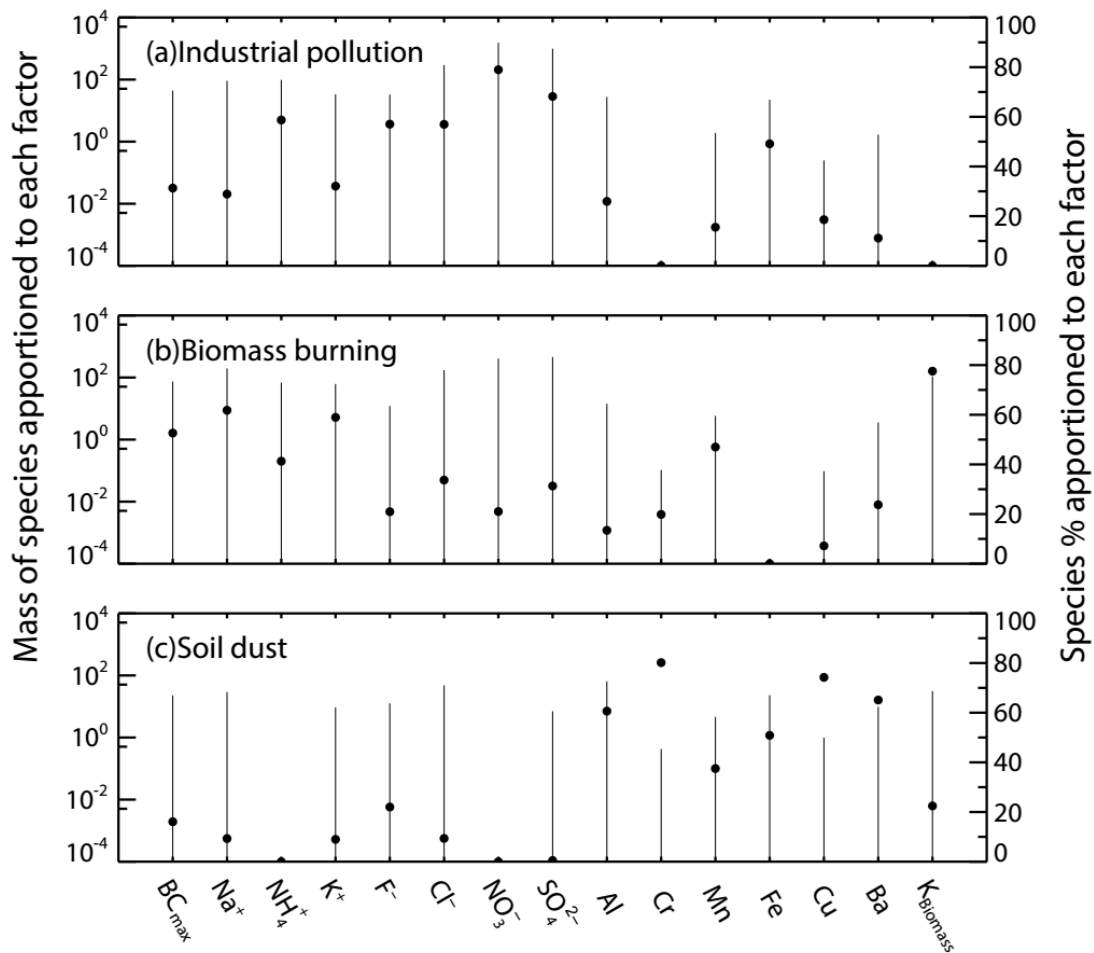
Fig. 5. Source profiles including the measured mass concentrations (lines) and the percent of components (dots) for the three factors/sources that were resolved by the PMF 5.0 model.
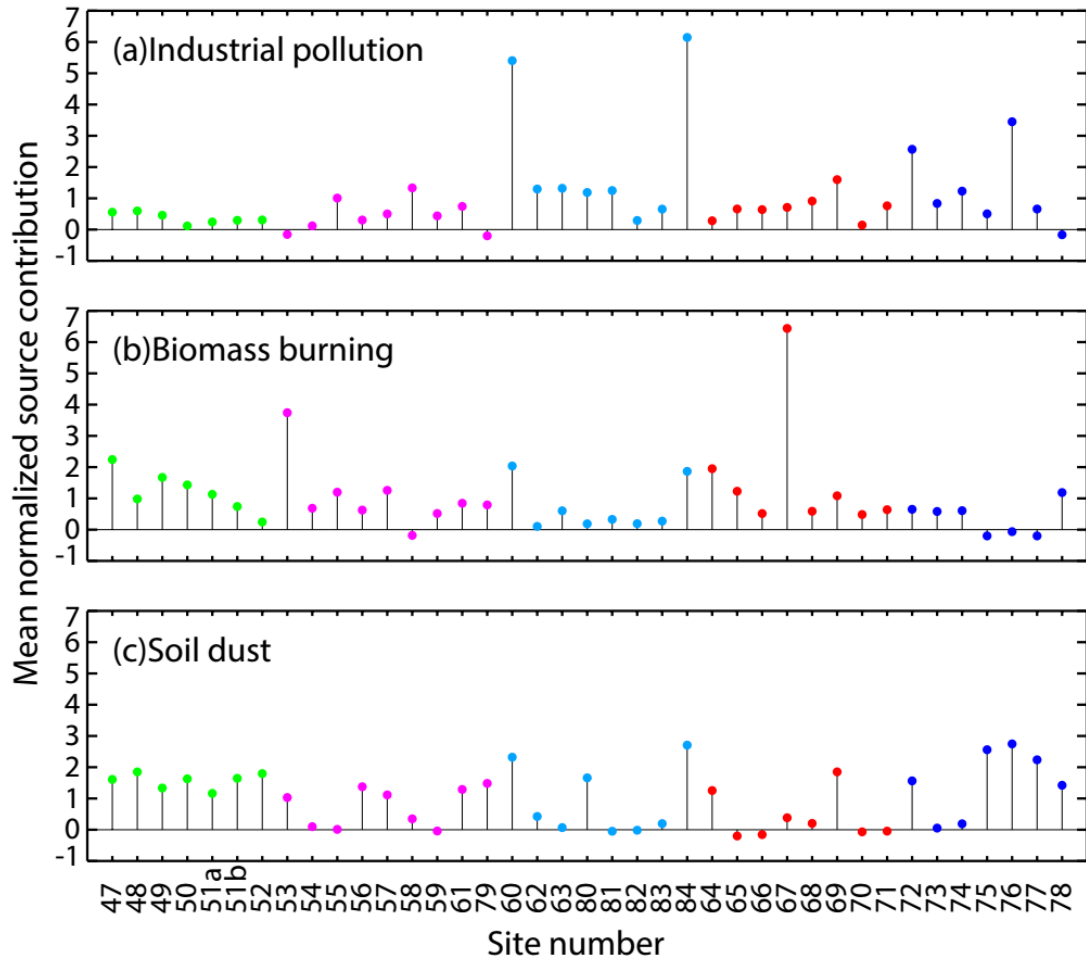
Fig. 6. Contributions from each source/factor to each sample or individual receptor site. The contributions have been normalized by the average value of the respective factor contributions over all sites.
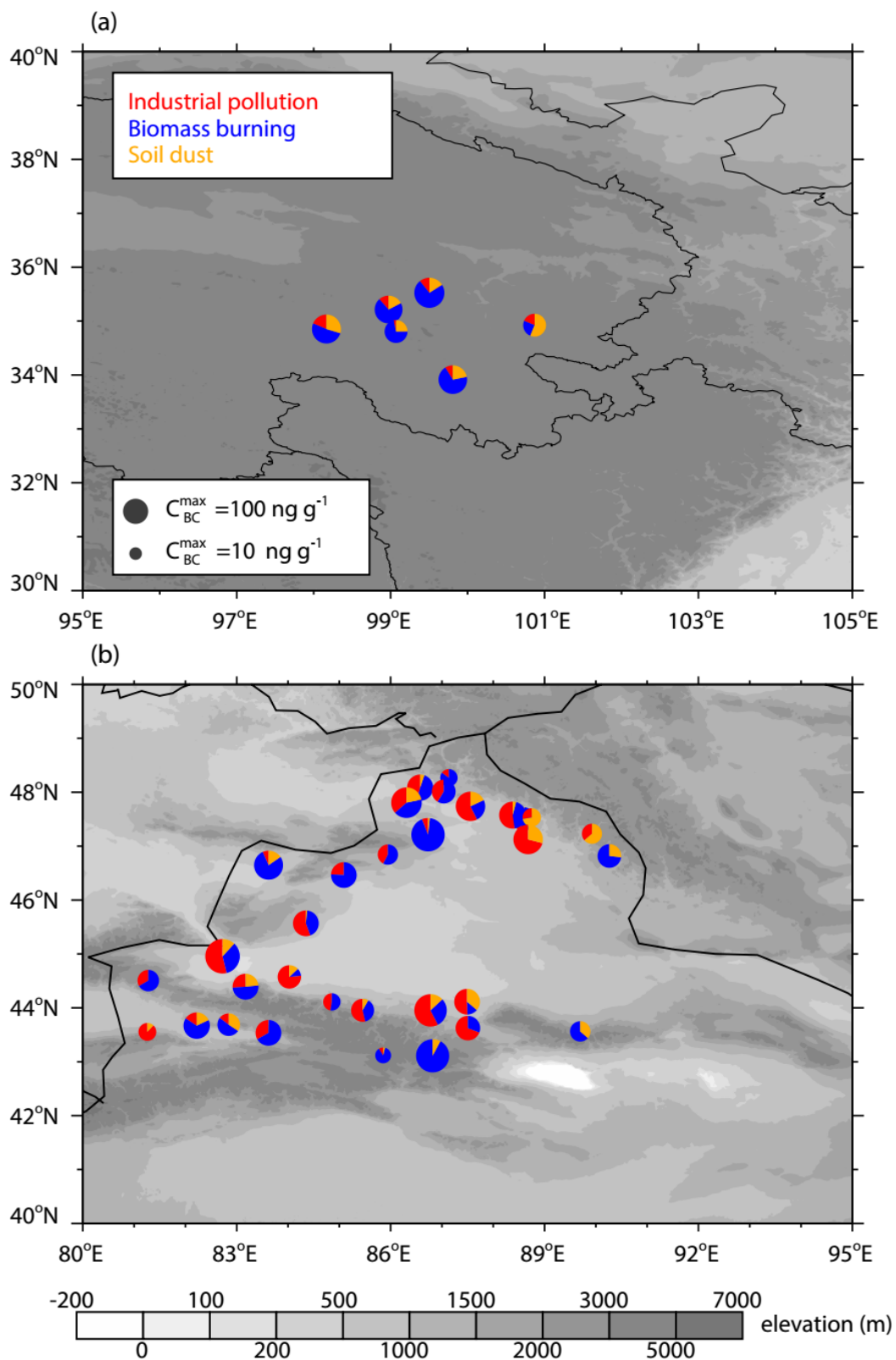
Fig. 7. Fractional contributions from soil dust, biomass burning, and industrial pollution to 650–700-nm particulate absorption according to the PMF analysis for the surface snow samples in (a) Qinghai and (b) Xinjiang.
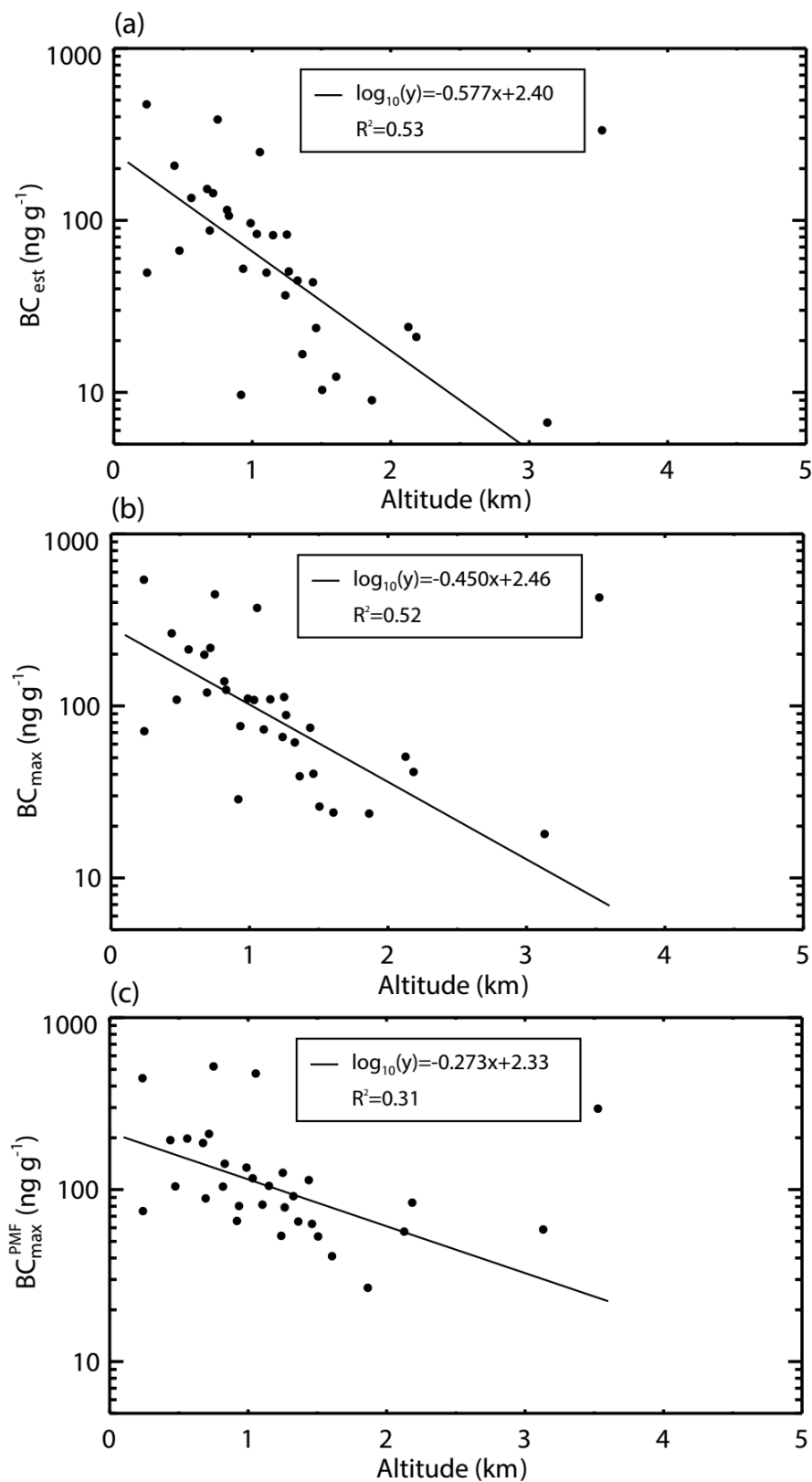
Fig. 8. (a) C_{BC}^{est} and (b) C_{BC}^{max} measured according to the ISSW and (C) C_{BC}^{max} determined by the PMF model for the surface snow for each site as a function of altitude for the sites in Xinjiang.
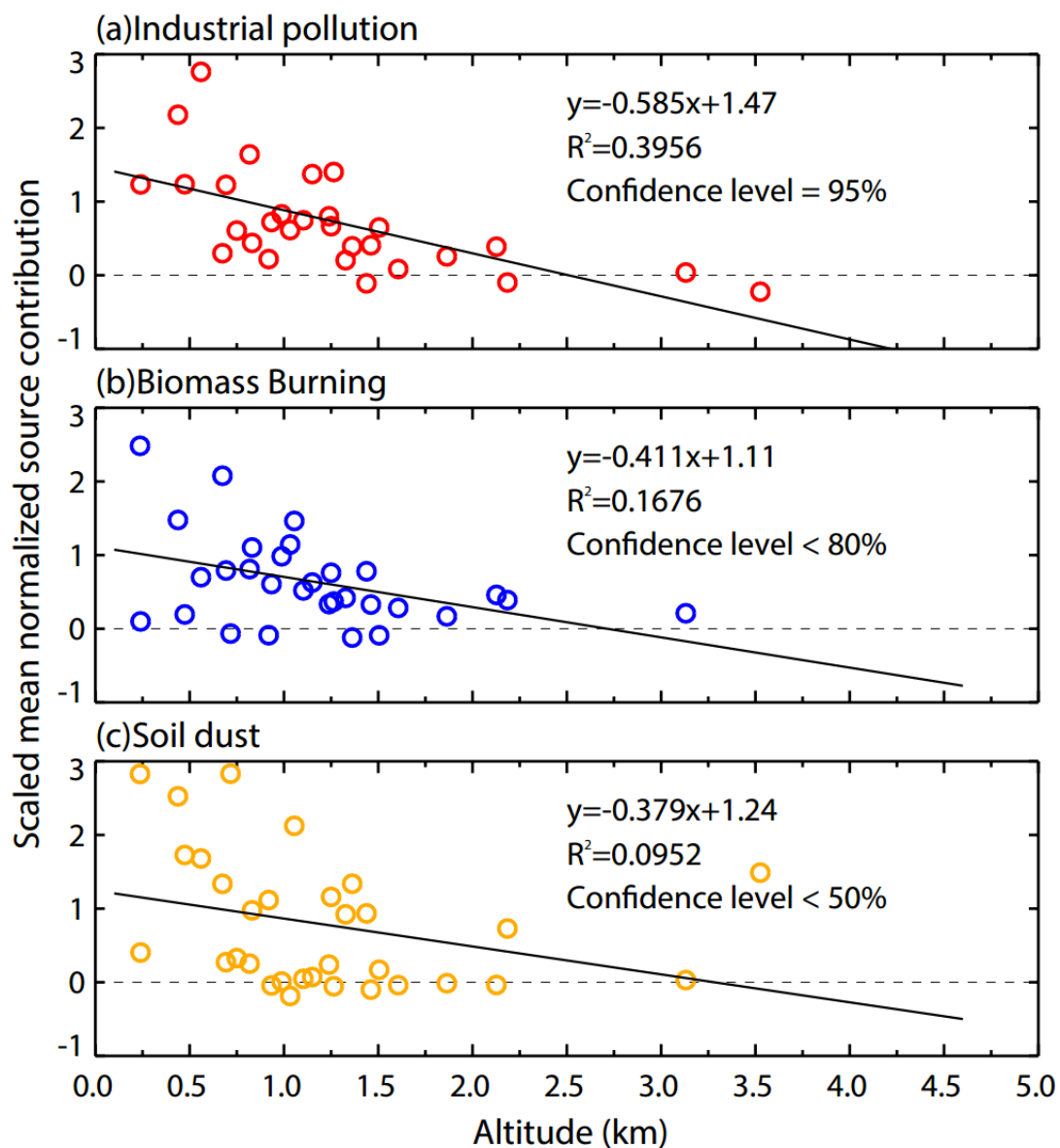
Fig. 9. Scaled contributions from each source/factor as a function of altitude at sampling sites in Xinjiang. The contributions were normalized by the average value of the respective factor contribution over all sites.
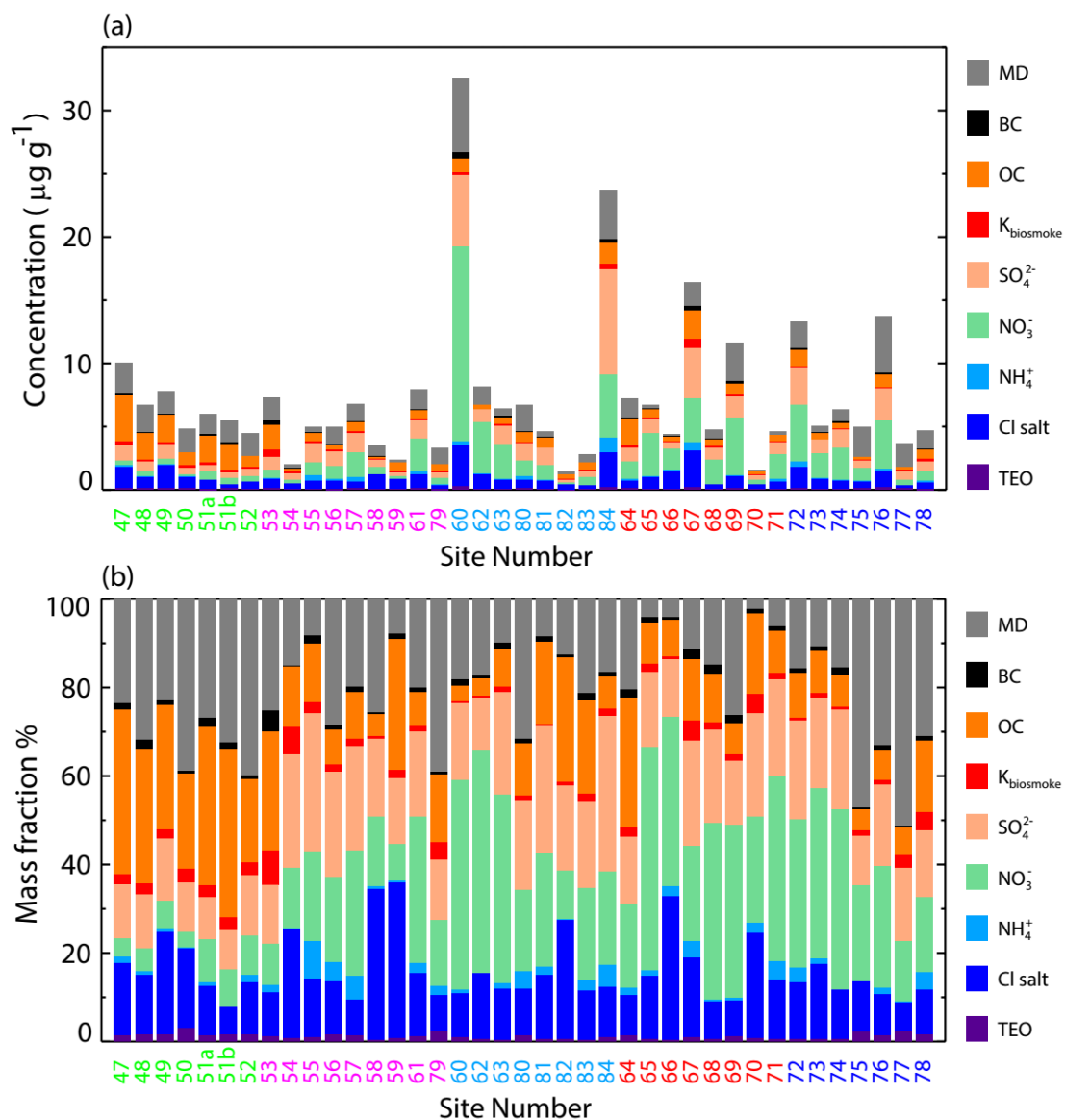
Fig. 10. (a) Average mass contributions and (b) average mass fractional contributions of the chemical components in the surface snow at each site.
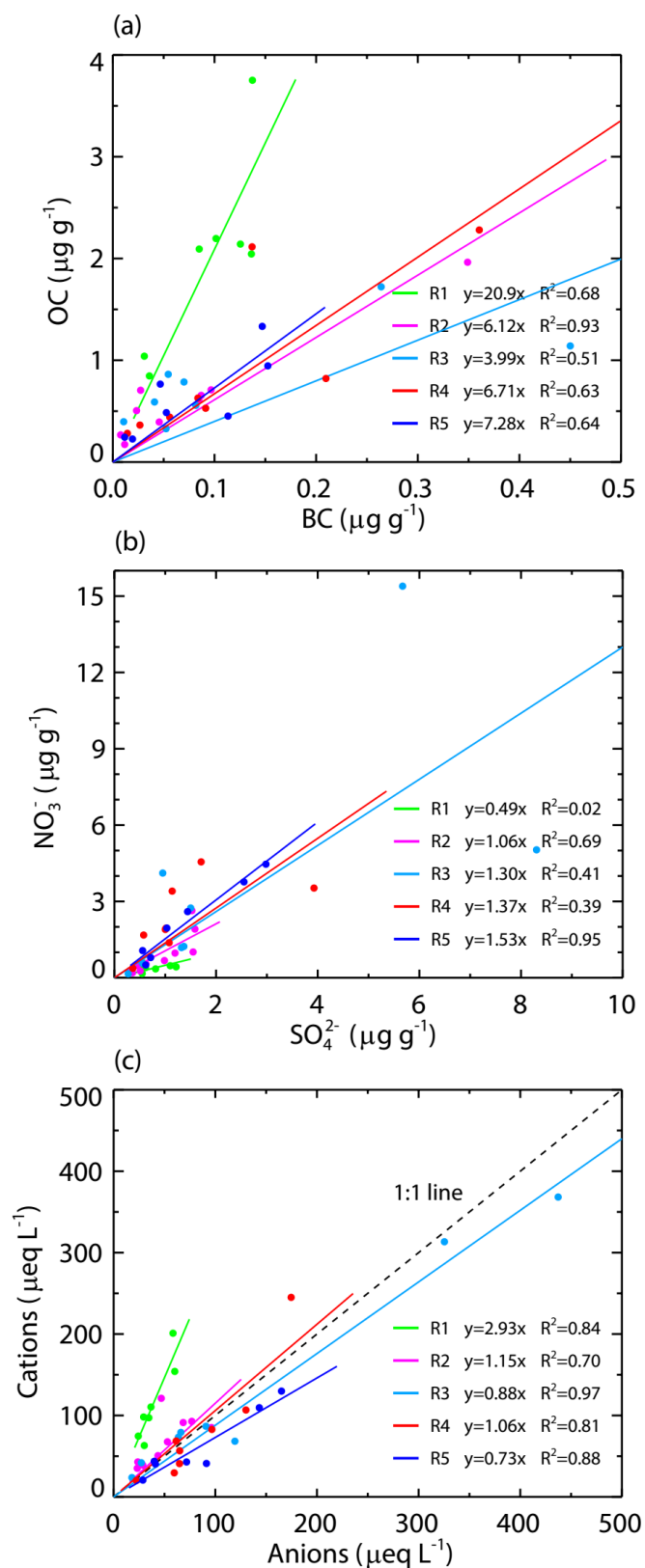
Fig. 11. Ratios of the (a) OC and BC mixing ratios and (b) NO_3^- and SO_4^{2-} concentrations, (c) and the charge balance between cations (Na^+, K^+, Ca^{2+}, Mg^{2+} and NH_4^+) and anions (SO_4^{2-}, NO_3^-, Cl^- and F^-) for the surface snow samples.

References

Alfaro, S. C., Lafon, S., Rajot, J. L., Formenti, P., Gaudichet, A., and Maille, M.: Iron oxides and light absorption by pure desert dust: An experimental study, J. Geophys. Res.-Atmos., 109, D8, 2004.

Amato, F., and Hopke, P. K.: Source apportionment of the ambient PM 2.5 across St. Louis using constrained positive matrix factorization, Atmos. Environ., 46, 329-337, 2012.

Amato, F., Pandolfi, M., Escrig, A., Querol, X., Alastuey, A., Pey, J., Perez, N., and Hopke, P.: Quantifying road dust resuspension in urban environment by multilinear engine: a comparison with PMF2, Atmos. Environ., 43, 2770-2780, 2009.

Andreae, M. O., and Merlet, P.: Emission of trace gases and aerosols from biomass burning, Global Biogeochem. CY., 15, 955-966, 2001.

Anttila, P., Paatero, P., Tapper, U., and Järvinen, O.: Source identification of bulk wet deposition in Finland by positive matrix factorization, Atmos. Environ., 29, 1705–1718, 1995.

Arimoto, R., Duce, R. A., Savoie, D. L., Prospero, J. M., Talbot, R., Cullen, J. D., Tomza, U., Lewis, N. F., and Jay, B. J.: Relationships among aerosol constituents from Asia and the North Pacific during PEM-West A, J. Geophys. Res.-Atmos., 101, 2011-2023, 1996.

Belis, C. A., Favez, O., Harrison, R. M., Larsen, B. R., Amato, F., El Haddad, I., Hopke, P. K., Nava, S., Paatero, P., Prévôt, A., Quass, U., et al.: European guide on air pollution source apportionment with receptor models., Publications Office, Luxembourg. [online] Available from: http://dx.publications.europa.eu/10.2788/9307 (Accessed 21 December 2016), 2014.

Bond, T. C., and Bergstrom, R. W.: Light Absorption by Carbonaceous Particles: An Investigative Review, Aerosol Sci. Tech., 40, 27-67, 2006.

Bond, T. C., Doherty, S. J., Fahey, D. W., Forster, P. M., Berntsen, T., DeAngelo, B. J., Flanner, M. G., Ghan, S., Karcher, B., Koch, D., Kinne, S., Kondo, Y., Quinn, P. K., Sarofim, M. C., Schultz, M. G., Schulz, M., Venkataraman, C., Zhang, H., Zhang, S., Bellouin, N., Guttikunda, S. K., Hopke, P. K., Jacobson, M. Z., Kaiser, J. W., Klimont, Z., Lohmann, U., Schwarz, J. P., Shindell, D., Storelvmo, T., Warren, S. G., and Zender, C. S.: Bounding the role of black carbon in the climate system: A scientific assessment, J. Geophys. Res.-Atmos., 118, 5380-5552, 2013.

Bond, T. C., Streets, D. G., Yarber, K. F., Nelson, S. M., Woo, J. H., and Klimont, Z.: A technology-based global inventory of black and organic carbon emissions from combustion, J. Geophys. Res.-Atmos., 109, D14203, 2004.

Brandt, R. E., Warren, S. G., and Clarke, A. D.: A controlled snowmaking experiment testing the relation between black carbon content and reduction of snow albedo, J. Geophys. Res., 116, D08109, 2011.

Cachier, H., and Pertuisot, M. H.: Particulate Carbon in Arctic Ice, Analusis, 22,

M34-M37, 1994.

Chen, L.-W. A., Watson, J. G., Chow, J. C., and Magliano, K. L.: Quantifying PM2. 5 source contributions for the San Joaquin Valley with multivariate receptor models, Environ. Sci. Technol., 41, 2818-2826, 2007.

Chylek, P., Johnson, B., Damiano, P. A., Taylor, K. C., and Clement, P.: Biomass Burning Record and Black Carbon in the Gisp2 Ice Core, Geophys. Res. Lett., 22, 89-92, 1995.

Chylek, P., Ramaswamy, V., and Srivastava, V.: Albedo of Soot-Contaminated Snow, J. Geophys. Res.-Oc. Atm., 88, 837-843, 1983.

Chylek, P., Srivastava, V., Cahenzli, L., Pinnick, R. G., Dod, R. L., Novakov, T., Cook, T. L., and Hinds, B. D.: Aerosol and Graphitic Carbon Content of Snow, J. Geophys. Res.-Atmos., 92, 9801-9809, 1987.

Clarke, A. D., and Noone, K. J.: Soot in the Arctic Snowpack - a Cause for Perturbations in Radiative-Transfer, Atmos. Environ., 19, 2045-2053, 1985.

Cong, Z. Y., Kang, S. C., Gao, S. P., Zhang, Y. L., Li, Q., and Kawamura, K.: Historical Trends of Atmospheric Black Carbon on Tibetan Plateau As Reconstructed from a 150-Year Lake Sediment Record, Environ. Sci. Technol., 47, 2579-2586, 2013.

Dall'Osto, M., Querol, X., Amato, F., Karanasiou, A., Lucarelli, F., Nava, S., Calzolai, G., and Chiari, M.: Hourly elemental concentrations in PM 2.5 aerosols sampled simultaneously at urban background and road site during SAPUSS–diurnal variations and PMF receptor modelling, Atmos. Chem. Phys., 13, 4375-4392, 2013.

Dang, C., and Hegg, D. A.: Quantifying light absorption by organic carbon in Western North American snow by serial chemical extractions, J. Geophys. Res.-Atmos., 119, 247-210, 2014.

Doherty, S. J., Dang, C., Hegg, D. A., Zhang, R., and Warren, S. G.: Black carbon and other light-absorbing particles in snow of central North America, J. Geophys. Res.-Atmos., 119, 807-812, 2014.

Doherty, S. J., Grenfell, T. C., Forsstrom, S., Hegg, D. L., Brandt, R. E., and Warren, S. G.: Observed vertical redistribution of black carbon and other insoluble light-absorbing particles in melting snow, J. Geophys. Res.-Atmos., 118, 5553-5569, 2013.

Doherty, S. J., Steele, M., Rigor, I., and Warren, S. G.: Interannual variations of light-absorbing particles in snow on Arctic sea ice, J. Geophys. Res.-Atmos., 120, 11391-11400, 2015.

Doherty, S. J., Warren, S. G., Grenfell, T. C., Clarke, A. D., and Brandt, R. E.: Light-absorbing impurities in Arctic snow, Atmos. Chem. Phys., 10, 11647-11680, 2010.

Eleftheriadis, K., Vratolis, S., and Nyeki, S.: Aerosol black carbon in the European Arctic: Measurements at Zeppelin station, Ny-Alesund, Svalbard from 1998-2007, Geophys. Res. Lett., 36, L02809, 2009.

Flanner, M. G., Zender, C. S., Hess, P. G., Mahowald, N. M., Painter, T. H., Ramanathan, V., and Rasch, P. J.: Springtime warming and reduced snow cover

from carbonaceous particles, Atmos. Chem. Phys., 9, 2481-2497, 2009.

Flanner, M. G., Zender, C. S., Randerson, J. T., and Rasch, P. J.: Present-day climate forcing and response from black carbon in snow, J. Geophys. Res., 112, D11202, 2007.Forsstrom, S., Strom, J., Pedersen, C. A., Isaksson, E., and Gerland, S.: Elemental carbon distribution in Svalbard snow, J. Geophys. Res.-Atmos., 114, D19112, 2009.

Gabbi, J., Huss, M., Bauder, A., Cao, F., and Schwikowski, M.: The impact of Saharan dust and black carbon on albedo and long-term mass balance of an Alpine glacier, Cryosphere, 9, 1385-1400, 2015.

Gianini, M. F. D., Fischer, A., Gehrig, R., Ulrich, A., Wichser, A., Piot, C., Besombes, J.-L., and Hueglin, C.: Comparative source apportionment of PM10 in Switzerland for 2008/2009 and 1998/1999 by Positive Matrix Factorisation, Atmos. Environ., 54, 149–158, 2012.

Grenfell, T. C., Doherty, S. J., Clarke, A. D., and Warren, S. G.: Light absorption from particulate impurities in snow and ice determined by spectrophotometric analysis of filters, Appl. Opt., 50, 2037-2048, 2011.

Grenfell, T. C., Light, B., and Sturm, M.: Spatial distribution and radiative effects of soot in the snow and sea ice during the SHEBA experiment, J. Geophys. Res.-Oceans, 107, C10, 2002.

Hadley, O. L., and Kirchstetter, T. W.: Black-carbon reduction of snow albedo, Nat. Clim. Change, 2, 437-440, 2012.

Hadley, O. L., Corrigan, C. E., Kirchstetter, T. W., Cliff, S. S., and Ramanathan, V.: Measured black carbon deposition on the Sierra Nevada snow pack and implication for snow pack retreat, Atmos. Chem. Phys., 10, 7505-7513, 2010.

Hagler, G. S. W., Bergin, M. H., Smith, E. A., and Dibb, J. E.: A summer time series of particulate carbon in the air and snow at Summit, Greenland, J. Geophys. Res.-Atmos., 112, D21309, 2007a.

Hagler, G. S. W., Bergin, M. H., Smith, E. A., Dibb, J. E., Anderson, C., and Steig, E. J.: Particulate and water-soluble carbon measured in recent snow at Summit, Greenland, Geophys. Res. Lett., 34, L16505, 2007b.

Hailin, W., ZHUANG, Y., Ying, W., Yele, S., Hui, Y., ZHUANG, G., and Zhengping, H.: Long-term monitoring and source apportionment of PM 2.5/PM 10 in Beijing, China, J. Environ. Sci., 20, 1323-1327, 2008.

Hansen, J., and Nazarenko, L.: Soot climate forcing via snow and ice albedos, Proc. Nat. Acad. Sci. U.S.A., 101, 423-428, 2004.

Hegg, D. A., Warren, S. G., Grenfell, T. C., Doherty, S. J., and Clarke, A. D.: Sources of light-absorbing aerosol in arctic snow and their seasonal variation, Atmos. Chem. Phys., 10, 10923-10938, 2010.

Hegg, D. A., Warren, S. G., Grenfell, T. C., Doherty, S. J., Larson, T. V., and Clarke, A. D.: Source Attribution of Black Carbon in Arctic Snow, Environ. Sci. Technol., 43, 4016-4021, 2009.

Hsu, S. C., Liu, S. C., Huang, Y. T., Chou, C. C. K., Lung, S. C. C., Liu, T. H., Tu, J. Y., and Tsai, F. J.: Long-range southeastward transport of Asian biosmoke pollution: Signature detected by aerosol potassium in Northern Taiwan, J.

Geophys. Res.-Atmos., 114, D14301, 2009.

Hsu, S. C., Liu, S. C., Tsai, F., Engling, G., Lin, I. I., Chou, C. K. C., Kao, S. J., Lung, S. C. C., Chan, C. Y., Lin, S. C., Huang, J. C., Chi, K. H., Chen, W. N., Lin, F. J., Huang, C. H., Kuo, C. L., Wu, T. C., and Huang, Y. T.: High wintertime particulate matter pollution over an offshore island (Kinmen) off southeastern China: An overview, J. Geophys. Res.-Atmos., 115, D17309, 2010.

Huang, J., Fu, Q., Zhang, W., Wang, X., Zhang, R., Ye, H., and Warren, S. G.: Dust and Black Carbon in Seasonal Snow Across Northern China, Bull. Amer. Meteor. Soc., 92, 175-181, 2011.

Huang, R. J., Zhang, Y., Bozzetti, C., Ho, K. F., Cao, J. J., Han, Y., Daellenbach, K. R., Slowik, J. G., Platt, S. M., Canonaco, F., Zotter, P., Wolf, R., Pieber, S. M., Bruns, E. A., Crippa, M., Ciarelli, G., Piazzalunga, A., Schwikowski, M., Abbaszade, G., Schnelle-Kreis, J., Zimmermann, R., An, Z., Szidat, S., Baltensperger, U., El Haddad, I., and Prevot, A. S.: High secondary aerosol contribution to particulate pollution during haze events in China, Nature, 514, 218-222, 2014.

IPCC: Climate Change 2013: The Physical Science Basis. Contribution of Working Group I to the Fifth Assessment Report of the Intergovernmental Panel on Climate Change, Stocker, T. F., Qin, D., Plattner, G.-K., Tignor, M., Allen, S. K., Boschung, J., Nauels, A., Xia, Y., Bex, V., and Midgley, P. M., Cambridge Univ. Press, Cambridge, United Kingdom and New York, NY, USA, 2013.

Jacobson, M. Z.: Climate response of fossil fuel and biofuel soot, accounting for soot's feedback to snow and sea ice albedo and emissivity, J. Geophys. Res.-Atmos., 109, D21201, 2004.

Jacobson, M. Z.: Control of fossil-fuel particulate black carbon and organic matter, possibly the most effective method of slowing global warming, J. Geophys. Res.-Atmos., 107, D19, 2002.

Jacobson, M. Z.: Strong radiative heating due to the mixing state of black carbon in atmospheric aerosols, Nature, 409, 695-697, 2001.

Kang, S. C., Zhang, Q. G., Kaspari, S., Qin, D. H., Cong, Z. Y., Ren, J. W., and Mayewski, P. A.: Spatial and seasonal variations of elemental composition in Mt. Everest (Qomolangma) snow/firn, Atmos. Environ., 41, 7208-7218, 2007.

Koch, D., Menon, S., Del Genio, A., Ruedy, R., Alienov, I., and Schmidt, G. A.: Distinguishing Aerosol Impacts on Climate over the Past Century, J. Climate, 22, 2659-2677, 2009.

Kulkarni, S.: Assessment of source-receptor relationships of aerosols: an integrated forward and backward modeling approach, 2009.

Lack, D. A. and Langridge, J. M.: On the attribution of black and brown carbon light absorption using the Ångström exponent, Atmos. Chem. Phys., 13, 10535-10543, 2013.

Lafon, S., Rajot, J. L., Alfaro, S. C., and Gaudichet, A.: Quantification of iron oxides in desert aerosol, Atmos. Environ., 38(8), 1211-1218, 2004.

Lafon, S., Sokolik, I. N., Rajot, J. L., Caquineau, S., and Gaudichet, A.: Characterization of iron oxides in mineral dust aerosols: Implications for light absorption, J. Geophys. Res.-Atmos., 111, D21, 2006.

Landis, M. S., Norris, G. A., Williams, R. W., and Weinstein, J. P.: Personal exposures to PM2.5 mass and trace elements in Baltimore, MD, USA, Atmos. Environ., 35, 6511-6524, 2001.

Li, C., Bosch, C., Kang, S., Andersson, A., Chen, P., Zhang, Q., Cong, Z., Chen, B., Qin, D., and Gustafsson, Ö.: Sources of black carbon to the Himalayan–Tibetan Plateau glaciers, Nat. Commun., 7, 12574, 2016.

McConnell, J. R., Edwards, R., Kok, G. L., Flanner, M. G., Zender, C. S., Saltzman, E. S., Banta, J. R., Pasteris, D. R., Carter, M. M., and Kahl, J. D. W.: 20th-century industrial black carbon emissions altered arctic climate forcing, Science, 317, 1381-1384, 2007.

Ming, J., Cachier, H., Xiao, C., Qin, D., Kang, S., Hou, S., and Xu, J.: Black carbon record based on a shallow Himalayan ice core and its climatic implications, Atmos. Chem. Phys., 8, 1343-1352, 2008.

Ming, J., Xiao, C. D., Cachier, H., Qin, D. H., Qin, X., Li, Z. Q., and Pu, J. C.: Black Carbon (BC) in the snow of glaciers in west China and its potential effects on albedos, Atmos. Res., 92, 114-123, 2009.

Oh, M.-S., Lee, T.-J., and Kim, D.-S.: Quantitative source apportionment of size-segregated particulate matter at urbanized local site in Korea, Aerosol Air Qual. Res., 11, 247-264, 2011.

Paatero, P., Hopke, P. K., Hoppenstock, J., and Eberly, S. I.: Advanced factor analysis of spatial distributions of PM2. 5 in the eastern United States, Environ. Sci. Technol., 37, 2460-2476, 2003.

Painter, T. H., Barrett, A. P., Landry, C. C., Neff, J. C., Cassidy, M. P., Lawrence, C. R., McBride, K. E., and Farmer, G. L.: Impact of disturbed desert soils on duration of mountain snow cover, Geophys. Res. Lett., 34, L12502, 2007.

Painter, T. H., Deems, J. S., Belnap, J., Hamlet, A. F., Landry, C. C., and Udall, B.: Response of Colorado River runoff to dust radiative forcing in snow, Proc. Nat. Acad. Sci. U.S.A., 107, 17125-17130, 2010.

Painter, T. H., Flanner, M. G., Kaser, G., Marzeion, B., VanCuren, R. A., and Abdalati, W.: End of the Little Ice Age in the Alps forced by industrial black carbon, Proc. Nat. Acad. Sci. U.S.A., 110, 15216-15221, 2013.

Peltoniemi, J. I., Gritsevich, M., Hakala, T., Dagsson-Waldhauserova, P., Arnalds, O., Anttila, K., Hannula, H. R., Kivekas, N., Lihavainen, H., Meinander, O., Svensson, J., Virkkula, A., and de Leeuw, G.: Soot on Snow experiment: bidirectional reflectance factor measurements of contaminated snow, Cryosphere, 9, 2323-2337, 2015.

Pio, C. A., Legrand, M., Oliveira, T., Afonso, J., Santos, C., Caseiro, A., Fialho, P., Barata, F., Puxbaum, H., Sanchez-Ochoa, A., Kasper-Giebl, A., Gelencser, A., Preunkert, S., and Schock, M.: Climatology of aerosol composition (organic versus inorganic) at nonurban sites on a west-east transect across Europe, J. Geophys. Res.-Atmos., 112, D23S02, 2007.

Pu, W., Wang, X., Zhang, X. Y., Ren, Y., Shi, J. S., Bi, J. R., and Zhang, B. D.: Size Distribution and Optical Properties of Particulate Matter (PM10) and Black Carbon (BC) during Dust Storms and Local Air Pollution Events across a Loess

Plateau Site, Aerosol Air Qual. Res., 15, 2212-2224, 2015.

Qian, Y., Gustafson, W. I., Leung, L. R., and Ghan, S. J.: Effects of soot-induced snow albedo change on snowpack and hydrological cycle in western United States based on Weather Research and Forecasting chemistry and regional climate simulations, J. Geophys. Res.-Atmos., 114, D03108, 2009.

Qiu, J.: China: the third pole, Nature News, 454, 393-396, 2008.

Ramanathan, V., and Carmichael, G.: Global and regional climate changes due to black carbon, Nat. Geosci., 1, 221-227, 2008.

Shindell, D., and Faluvegi, G.: Climate response to regional radiative forcing during the twentieth century, Nat. Geosci., 2, 294-300, 2009.

Shindell, D. T., Chin, M., Dentener, F., Doherty, R. M., Faluvegi, G., Fiore, A. M., Hess, P., Koch, D. M., MacKenzie, I. A., Sanderson, M. G., Schultz, M. G., Schulz, M., Stevenson, D. S., Teich, H., Textor, C., Wild, O., Bergmann, D. J., Bey, I., Bian, H., Cuvelier, C., Duncan, B. N., Folberth, G., Horowitz, L. W., Jonson, J., Kaminski, J. W., Marmer, E., Park, R., Pringle, K. J., Schroeder, S., Szopa, S., Takemura, T., Zeng, G., Keating, T. J., and Zuber, A.: A multi-model assessment of pollution transport to the Arctic, Atmos. Chem. Phys., 8, 5353-5372, 2008.

Thevenon, F., Anselmetti, F. S., Bernasconi, S. M., and Schwikowski, M.: Mineral dust and elemental black carbon records from an Alpine ice core (Colle Gnifetti glacier) over the last millennium, J. Geophys. Res.-Atmos., 114, D17102, 2009.

Thompson, L. G., Yao, T., Mosley-Thompson, E., Davis, M. E., Henderson, K. A., and Lin, P. N.: A high-resolution millennial record of the South Asian Monsoon from Himalayan ice cores, Science, 289, 1916-1919, 2000.

Waked, A., Favez, O., Alleman, L. Y., Piot, C., Petit, J.-E., Delaunay, T., Verlinden, E., Golly, B., Besombes, J.-L., Jaffrezo, J.-L. and Leoz-Garziandia, E.: Source apportionment of PM10 in a north-western Europe regional urban background site (Lens, France) using positive matrix factorization and including primary biogenic emissions, Atmos. Chem. Phys., 14(7), 3325–3346, 2014.

Wang, H., and Han, G. L.: Chemical composition of rainwater and anthropogenic influences in Chengdu, Southwest China, Atmos. Res., 99, 190-196, 2011.

Wang, X., Doherty, S. J., and Huang, J.: Black carbon and other light-absorbing impurities in snow across Northern China, J. Geophys. Res.-Atmos., 118, 1471-1492, 2013.

Wang, X., Pu, W., Ren, Y., Zhang, X., Zhang, X., Shi, J., Jin, H., Dai, M., and Chen, Q.: Observations and model simulations of snow albedo reduction in seasonal snow due to insoluble light-absorbing particles during 2014 Chinese survey, Atmos. Chem. Phys., 2017.

Wang, X., Pu, W., Zhang, X., Ren, Y., and Huang, J.: Water-soluble ions and trace elements in surface snow and their potential source regions across northeastern China, Atmos. Environ., 114, 57-65, 2015.Wang, X., Xu, B. Q., and Ming, J.: An Overview of the Studies on Black Carbon and Mineral Dust Deposition in Snow and Ice Cores in East Asia, J. Meteorol. Res., 28, 354-370, 2014.

Warren, S. G., and Wiscombe, W. J.: A Model for the Spectral Albedo of Snow .2.

Snow Containing Atmospheric Aerosols, J. Atmos. Sci., 37, 2734-2745, 1980.

Warren, S. G.: Impurities in Snow - Effects on Albedo and Snowmelt Review, Ann. Glaciol., 5, 177-179, 1984.

Wedepohl, K. H.: The Composition of the Continental-Crust, Geochim. Cosmochim. Acta, 59, 1217-1232, 1995.

Xie, S., Liu, Z., Chen, T., and Hua, L.: Spatiotemporal variations of ambient PM 10 source contributions in Beijing in 2004 using positive matrix factorization, Atmos. Chem. Phys., 8, 2701-2716, 2008.

Xu, B. Q., Cao, J. J., Hansen, J., Yao, T. D., Joswia, D. R., Wang, N. L., Wu, G. J., Wang, M., Zhao, H. B., Yang, W., Liu, X. Q., and He, J. Q.: Black soot and the survival of Tibetan glaciers, Proc. Nat. Acad. Sci. U.S.A., 106, 22114-22118, 2009.

Xu, B. Q., Cao, J. J., Joswiak, D. R., Liu, X. Q., Zhao, H. B., and He, J. Q.: Post-depositional enrichment of black soot in snow-pack and accelerated melting of Tibetan glaciers, Environ. Res. Lett., 7, 014022, 2012.

Xu, B. Q., Yao, T. D., Liu, X. Q., and Wang, N. L.: Elemental and organic carbon measurements with a two-step heating-gas chromatography system in snow samples from the Tibetan Plateau, Ann. Glaciol., 43, 257-262, 2006.

Xu, J., Zhang, Q., Li, X., Ge, X., Xiao, C., Ren, J., and Qin, D.: Dissolved Organic Matter and Inorganic Ions in a Central Himalayan Glacier-Insights into Chemical Composition and Atmospheric Sources, Environ. Sci. Technol., 47, 6181-6188, 2013.

Yan, X. Y., Ohara, T., and Akimoto, H.: Bottom-up estimate of biomass burning in mainland China, Atmos. Environ., 40, 5262-5273, 2006.

Ye, H., Zhang, R., Shi, J., Huang, J., Warren, S. G., and Fu, Q.: Black carbon in seasonal snow across northern Xinjiang in northwestern China, Environ. Res. Lett., 7, 044002, 2012.

Yesubabu, V., Srinivas, C. V., Hariprasad, K. B. R. R., and Baskaran, R.: A Study on the Impact of Observation Assimilation on the Numerical Simulation of Tropical Cyclones JAL and THANE Using 3DVAR, Pure Appl. Geophys., 171, 2023-2042, 2014.

Zhang, R., Hegg, D. A., Huang, J., and Fu, Q.: Source attribution of insoluble light-absorbing particles in seasonal snow across northern China, Atmos. Chem. Phys., 13, 6091-6099, 2013a.

Zhang, R., Jing, J., Tao, J., Hsu, S. C., Wang, G., Cao, J., Lee, C. S. L., Zhu, L., Chen, Z., Zhao, Y., and Shen, Z.: Chemical characterization and source apportionment of PM2.5 in Beijing: seasonal perspective, Atmos. Chem. Phys., 13, 7053-7074, 2013b.

Zhao, C., Hu, Z., Qian, Y., Leung, L. R., Huang, J., Huang, M., Jin, J., Flanner, M. G., Zhang, R., Wang, H., Yan, H., Lu, Z., and Streets, D. G.: Simulating black carbon and dust and their radiative forcing in seasonal snow: a case study over North China with field campaign measurements, Atmos. Chem. Phys., 14, 11475-11491, 2014.